Research Article

Derivation of Jurassic HIMU-like intraplate basalts from mantle transition zone in South China: New geochemical constraints from olivine-hosted melt inclusion

Yangming Wu [a,b], Feng Guo [a,*], Xuan-Ce Wang [c], Simon A. Wilde [c,d], Weiming Fan [e]

[a] State Key Laboratory of Isotope Geochemistry, Guangzhou Institute of Geochemistry, Chinese Academy of Sciences, Guangzhou 510640, China
[b] College of Earth Sciences, University of Chinese Academy of Sciences, Beijing 100049, China
[c] Research Centre for Earth System Science, Yunnan University, Kunming 650500, China
[d] The Institute for Geoscience Research (TIGeR), School of Earth and Planetary Sciences, Curtin University, GPO Box, U1987, Perth, WA, 6845, Australia
[e] Institute of Tibet Plateau Research, Chinese Academy of Sciences, Beijing 100101, China

ABSTRACT

The petrogenesis of high-μ (HIMU, $\mu = {}^{238}U/{}^{204}Pb$) basalt in a continental setting remains highly controversial. Here we present a comprehensive geochemical (including major and trace element and isotopic compositions of whole-rock, olivine and melt inclusion) data on Jurassic HIMU-like basalts from the interior (Antang) of South China. This study identified high-H_2O (up to 5.0 wt%) olivine-hosted melt inclusions in these basalts. After stripping off the effects of degassing, post-entrapment crystallization and kinetic diffusion, the primary magma of the Antang basalts was estimated to contain ≥2.65 wt% H_2O and the corresponding mantle source contains >1000 ppm H_2O, which is much higher than the water content of convecting asthenosphere and lower mantle. In addition, the relative depletion of fluid-mobile elements and positive Nb-Ta anomalies in bulk rocks and melt inclusions, and the distance far away from the contemporaneous paleo-Pacific subduction zone, preclude an origin from a slab fluid-metasomatized mantle. The strong depletion of CaO in both olivine phenocrysts and whole-rock compositions further indicates that the basaltic magmas originated from an eclogitic or pyroxenitic mantle source. The combined geochemical data suggest that the Antang basalts were most likely derived from a hydrous source, which was composed mainly of ancient recycled oceanic crust that had stagnated in the mantle transition zone (MTZ) for more than one billion years. Our results therefore provide a new perspective on the MTZ origin of intracontinental basalts and imply that the hydrous MTZ can preserve recycled crustal components for long periods of time and form distinct mantle reservoirs for intraplate basalts.

© 2019 Elsevier B.V. All rights reserved.

1. Introduction

High-μ (HIMU, $\mu = {}^{238}U/{}^{204}Pb$) basalt refers to a group of oceanic island mafic lavas with very high $^{206}Pb/^{204}Pb$ ratios, coupled with low $^{87}Sr/^{86}Sr$ and moderate $^{143}Nd/^{144}Nd$ ratios, suggesting an unusual mantle source characterized by long-term U and Th enrichment relative to Pb without an associated increase in Rb/Sr (Zindler and Hart, 1986). HIMU basalts from different localities have remarkably uniform trace element features, such as Nb and Ta enrichment relative to other incompatible elements and depletion in highly incompatible elements (e.g., Cs, Rb, and Ba) and fluid-mobile elements (e.g., K, Pb, and Sr) (e.g., Kogiso et al., 1997b; Thirlwall, 1997). Debate continues regarding the origin of HIMU, with an origin from either metasomatized lithospheric mantle (e.g., Pilet et al., 2008; Weiss et al., 2016) or dehydrated

altered oceanic crust (e.g., Chauvel et al., 1992; Weaver, 1991), which undergoes long-term isolation from the convective mantle (Hanyu et al., 2011; Stracke et al., 2003; Thirlwall, 1997). An origin from partial melting of subducted oceanic slabs that have been buried in the deep mantle has been also proposed to explain the hotspot/plume-related HIMU basalts, such as at St. Helena, Mangaia, and Tubuaii (e.g., Chauvel et al., 1992; Hanyu et al., 2011; Hofmann, 1997). In contrast, the lack of evidence for the presence of plume activities (e.g., large-scale doming, linear space-time trends of volcanic centers, and large volumes of erupted magmas) let to argue against a plume origin for many HIMU-type alkaline magmas that erupted in continental settings (e.g., Hoernle et al., 2006; Panter et al., 2006).

Seismic tomography shows that the intraplate HIMU-like basalts in the Mediterranean area are related to a prominent low-velocity anomaly with a plume-like shape rooted within the mantle transition zone (MTZ) (Vinnik and Farra, 2007). The upwelling of transition zone materials, which have been stagnated for a long period of time, has been

proposed to explain the mantle source of lamproites from Gaussberg in the East Antarctic shield (Murphy et al., 2002) and an Enriched Mantle-1 (EM1) feature of Cenozoic potassic basalts from NE China (Kuritani et al., 2011, 2013; Wang et al., 2017). As mixing and petrological homogenization processes are less efficient in the MTZ than in the upper and lower mantle, the MTZ may be heterogeneous and contain discrete lithological domains of former subducted oceanic crust (e.g., Kuritani et al., 2011; Ringwood, 1994). The long-term storage of recycled ancient dehydrated oceanic crust in the MTZ thus has the potential to represent a HIMU-like mantle reservoir. HIMU-like basalts can therefore help to identify recycled crustal components in the deep Earth and to understand the mechanism for the long-term preservation of mantle reservoirs.

Several petrological and geochemical indexes can be used to determine the mantle source of HIMU-like basalts. For example, experimental studies on mantle melting have demonstrated that melt derived from a metasomatized lithospheric mantle (amphibole/phlogopite-bearing peridotite) has a distinct chemical composition from that derived from recycled oceanic crust (eclogite and/or pyroxenite) (e.g., Kogiso and Hirschmann, 2006; Pilet et al., 2008). Moreover, the distinct water distribution in Earth's mantle may provide a new constraint on the mantle source of basalts. The mantle transition zone (MTZ) is proposed to be hydrated and acts as a huge tank in Earth's deep-water cycle (Karato, 2010; Wang et al., 2015, 2016) in accordance with geophysical observations (Meier et al., 2009), electrical-conductivity experiments (Huang et al., 2005), and mineral inclusions in diamonds (Pearson et al., 2014). Whereas, the convecting asthenosphere (Saal et al., 2002) and lower mantle (e.g., Bolfan-Casanova et al., 2002, 2003) are considered to have much lower H_2O contents than the MTZ. Thus, basalts derived from different mantle layers may contain distinct water contents. In addition, hydrogen isotopes will be fractionated during oceanic slab subduction. Studies on hydrous minerals in subaerial arc rocks, such as amphibole, point to a high δD source for magmatic water (ranging from −45 to −20‰) (Miyagi and Matsubaya, 2003). Thus, lithospheric mantle metasomatized by dehydration of subducting slab will have relatively higher hydrogen isotopes than the pristine mantle, which is contrary to the dehydrated recycled slab (Shaw et al., 2008; Xu et al., 2014). Therefore, the water content and hydrogen isotope of mantle-derived primary melts may be one of the important indexes to identify a HIMU source.

Because olivine is an early crystallizing phase in basalts, olivine-hosted melt inclusions should best represent primary magmas in equilibrium with their mantle sources (e.g., Danyushevsky et al., 2000;). In this paper, we conducted a comprehensive geochemical study of the Mesozoic intraplate basalts with HIMU-like features in the interior (Antang) of South China, including *in situ* element and H-O isotope analyses on olivines and their melt inclusions, together with major, trace element and Sr-Nd-Pb-Hf-Os isotope analyses of whole-rock samples. This new dataset enables us to estimate the water content and composition of primary mantle-derived magma and to constrain the source lithology, and provides new perspectives on the origin of intraplate basalts in the light of deep water cycling.

2. Geological background and sample descriptions

The South China Block (SCB) is divided into the Cathaysia Block in the southeast and the Yangtze Craton in the northwest (Fig. 1). The Yangtze Craton consists of an Archean-Paleoproterozoic basement, including the 3.3–2.9 Ga Kongling Complex in the Yangtze Gorge area (Gao et al., 2011). Basement outcrops in the Cathaysian Block include the Badu, Chencai and Baoban complexes, with formation ages from Paleoproterozoic to Mesoproterozoic (Yu et al., 2007). The Yangtze and Cathaysia blocks were amalgamated to form the unified SCB during the Neoproterozoic Sibao orogeny (~1.0–0.8 Ga) (Li et al., 2009).

Igneous activity in South China has been voluminous since the Mesozoic (Zhou et al., 2006). The intense magmatism, lithospheric

deformation, and metal mineralization initiated since middle Permian, possibly related to subduction of the paleo-Pacific Oceanic Plate beneath East Asia (Li et al., 2012). The Mesozoic volcanic lavas in South China are predominantly felsic in composition (95%) with subordinate mafic magmas (<5%) (Zhou et al., 2006). The Jurassic basaltic lavas are sporadically distributed across the Cathaysia Block, including the Ningyuan, Antang, Daoxian, Yizhang, Chenlong, Huilongyu, Zhaibei, Fankeng, Baimianshan, and Dongkeng (Fig. 1).

Antang village is located along the Chenzhou-Linwu Fault in the Cathaysia Block, south of the Jiangshan-Shaoxing Fault (Fig. 1). The Jurassic Antang basalts (168 Ma) (Wang et al., 2004) are fresh, dark green in colour with euhedral to subhedral olivine (~10%) and lesser clinopyroxene phenocrysts (<4%) up to 1.0 mm in size in a dominantly aphanitic groundmass, composed of microcrystalline olivine, clinopyroxene, plagioclase and Fe-Ti oxides. Melt inclusions are preserved in olivine and occur as droplets <50 μm in size, comprising glass, vapour bubbles and microcrystalline clinopyroxene and olivine (Fig. 2).

3. Analytical techniques

3.1. Whole-rock major and trace element analyses

Seven fresh basalt samples were collected from Antang village (27°0′43.2′′N; 114°42′38.5′′E) for whole-rock geochemical and isotopic analyses. These rock samples were cut into millimeter-scale chips and removed weathered rims. After washed in 3% HCl and cleaned with de-ionized water, these chips were crushed into small fragments (<0.5 cm in diameter) in a corundum crusher and then reduced to 200 mesh in an agate ring mill. All analyses were undertaken at the State Key Laboratory of Isotope Geochemistry, Guangzhou Institute of Geochemistry, Chinese Academy of Sciences (GIGCAS). One randomly selected sample (JA16-12R) was performed to monitor the data quality and reproducibility. Whole-rock major oxides were determined using a Rigaku RIX 2000 X-ray fluorescence spectrometer (XRF) on fused glass disks, with analytical errors less than 3% for SiO_2, Al_2O_3, Fe_2O_3, MgO, CaO, Na_2O and K_2O, and less than 5% for TiO_2, MnO and P_2O_5. Trace element analyses were carried out using a Perkin-Elmer ELAN 6000 inductively coupled plasma mass spectrometer (ICP-MS). The analytical precision is generally better than 5% for element with concentrations >200 ppm, and 5–10% when less than 200 ppm.

3.2. Whole-rock Sr-Nd-Pb-Hf-Os isotope analyses

Whole-rock Sr-Nd-Pb-Hf isotopic compositions were determined using a Neptune multi-collector ICP-MS (MC-ICP-MS). The measured $^{87}Sr/^{86}Sr$ and $^{143}Nd/^{144}Nd$ ratios were normalized to $^{86}Sr/^{88}Sr = 0.1194$ and $^{146}Nd/^{144}Nd = 0.7219$, respectively. Reference standards were analyzed along with samples and gave $^{87}Sr/^{86}Sr = 0.710297 \pm 8$ (2σ, n = 7) for NBS987 and $^{143}Nd/^{144}Nd = 0.512101 \pm 5$ (2σ, n = 7) for JNdi-1 (0.512115 ± 5). For Pb isotopic analyses, 150 mg of rock powder was placed into a Teflon vessel and dissolved in an HNO_3 + HF mixture for three days. Pb was separated and purified by conventional anion exchange techniques (AG1X8, 200–400 resin) with diluted HBr as eluant. The internal correction performed for the Pb isotopic analyses uesed a thallium solution. Repeated measurements of standard NBS981 yielded $^{206}Pb/^{204}Pb = 16.9311 \pm 4$ (2σ, n = 8), $^{207}Pb/^{204}Pb = 15.4838 \pm 5$ (2σ, n = 8) and $^{208}Pb/^{204}Pb = 36.6757 \pm 14$ (2σ, n = 8). For Hf isotope analyses, the $^{176}Hf/^{177}Hf$ ratios were normalized to $^{179}Hf/^{177}Hf = 0.7325$. The reported $^{176}Hf/^{177}Hf$ ratios were adjusted to the standard solution JMC-475 of 0.282160. The reference standard gave $^{176}Hf/^{177}Hf = 0.282184 \pm 4$ (2σ, n = 9). Analyses of the USGS reference material BHVO-2 yielded $^{87}Sr/^{86}Sr = 0.703511 \pm 9$ (n = 5), $^{143}Nd/^{144}Nd = 0.512972 \pm 5$ (n = 5), $^{206}Pb/^{204}Pb = 18.6468 \pm 6$ (n = 5), $^{207}Pb/^{204}Pb = 15.5221 \pm 6$ (n = 5), $^{208}Pb/^{204}Pb = 38.1957 \pm 17$ (n = 5) and $^{176}Hf/^{177}Hf = 0.283093 \pm 4$ (n = 5), being in agreement
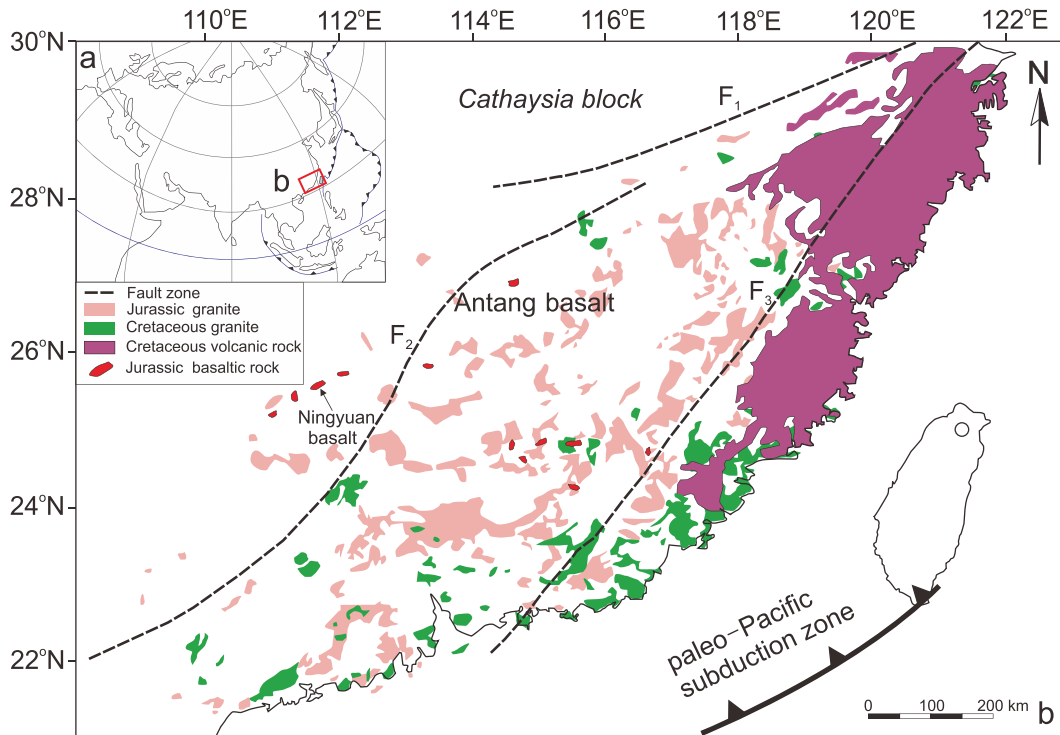
Fig. 1. A geologic map showing the distributions of Mesozoic magmatic rocks and major faults in Southeast China (Wang et al., 2008; Zhou et al., 2006). Inset figure shows a simplified tectonic map of China with a speculated subduction zone of the Paleo-Pacific slab in the late Mesozoic. The Antang basalt is located ~800 km west of the paleo-Pacific subduction zone.

with the recommended values of $^{87}Sr/^{86}Sr = 0.703481 \pm 20$, $^{143}Nd/^{144}Nd = 0.512983 \pm 10$, $^{206}Pb/^{204}Pb = 18.6173 \pm 465$, $^{207}Pb/^{204}Pb = 15.5355 \pm 54$ and $^{208}Pb/^{204}Pb = 38.2108 \pm 384$ and $^{176}Hf/^{177}Hf = 0.283096 \pm 20$ (Weis et al., 2005). The blanks were generally <100 pg for Sr and <50 pg for Nd, Pb and Hf.

The basaltic samples chosen for Re-Os isotope analyses were carefully fragmented into chips (<0.5 cm), and then leached and cleaned in 3% HCl for half an hour. The Re concentrations were measured by isotope dilution-inductively coupled plasma-mass spectrometry (ID-ICP-MS, Thermo-Scientific X2). The isotopic abundance of OsO_3^- and ReO_4^- were measured on a thermal ionization mass spectrometer (TIMS, Thermo TRITON). The detailed procedure was described in Li et al. (2014). Total blank levels were 1.9 ± 4.2 pg (2σ) and 0.58 ± 0.02 pg (2σ) for Re and Os, respectively, with an $^{187}Os/^{188}Os$ ratio of 0.1109 ± 0.005 (2σ). The reference basalt BIR-1 was also analyzed in the analytical batch, yielding Re = 687 ± 25 ppt, Os = 362 ± 13 ppt, and $^{187}Os/^{188}Os = 0.1338 \pm 2$, in good agreement with the published data for BIR-1 (Re = 675 ± 7; Os = 355 ± 20; $^{187}Os/^{188}Os = 0.1337 \pm 4$; Ishikawa et al., 2014). The different Re and Os concentrations and $^{187}Os/^{188}Os$ for repeated analyses of the same samples are possibly related to the nugget effect (Reisberg and Meisel, 2002).

3.3. In situ chemical and oxygen isotope analyses of olivine

The chemical composition of olivine was determined by electron probe micro-analyses (EPMA) using a JEOL JXA-8100 at GIGCAS. Olivine analyses followed the procedures of Sobolev et al. (2007). The operating conditions for olivine analyses were an accelerating voltage of 20 kV, a probe current of 3.0×10^{-7} A and a spot size of 3 μm. An internal olivine standard (from mantle xenolith, Hannuoba) was analyzed before and after each batch (every five samples) of analyses. The relative errors for the olivine standard were less than 1% for major elements (SiO_2, MgO and FeO), and 4.5% for minor elements (CaO, MnO and NiO) (Table S1a).

Oxygen isotopic compositions of olivine were analyzed with a CAMECA HR-IMS-1280 ion microprobe at GIGCAS. The Cs^+ primary

beam was accelerated at 10 kV with an intensity of ca. 2.0 nA. The spot size was about 20 μm in diameter (10 μm beam diameter + 10 μm raster). An electron gun was used to compensate for sample charging during analyses. Secondary ions were extracted with a −10 kV potential. Oxygen isotopes were measured in multi-collector mode with two off-axis Faraday cups with each analysis consisting of 20 cycles×4 counting time. The external reproducibility of the standard (San Carlos) for $\delta^{18}O$ was 0.4‰ (2σ), which was set as the error for individual measurements. Measured $^{18}O/^{16}O$ ratios were normalized using the Vienna Standard Mean Ocean Water composition (VSMOW, $^{18}O/^{16}O = 0.0020052$), and then corrected for instrumental mass fractionation (IMF). Then the $\delta^{18}O$ for samples were corrected by the equation: $\delta^{18}O_{sample} = \delta^{18}O_{measured} + IMF$. Many studies have shown that the impact of mass fractionation (IMF) of SIMS oxygen isotope analysis on olivine could be negligible providing that the olivine has Fo number ranging from 70 to 92 (e.g., Guo et al., 2013; Wang et al., 2015). Thus, the potential IMF effect, especially for olivine with Fo >80, should be negligible.

3.4. Major and trace element analyses of homogenized melt inclusion (HMI)

To obtain the chemical composition of olivine-hosted melt inclusions, it is preferable to analyze a homogenized glass rather than a mixture of various crystalline phases and residual glass (Danyushevsky et al., 2000). Prior to analysis, a 1.0 atm gas-mixing furnace was used to heat the olivine grains to 1250°C at the quartz-fayalite-magnetite buffer. The platinum packet was then rapidly raised back to the top of the furnace tube after being heated for 10 min to achieve homogenization of the glassy inclusions. Then the host olivine was embedded in epoxy resin and polished on one side until the melt inclusions were exposed. Well-preserved melt inclusions with a diameter larger than 30 μm were chosen for analysis. Major element compositions of the homogenized melt inclusions were analysed by EPMA with a JEOL JXA-8100 Electron Microprobe following the procedure reported by Wang and Gaetani (2008). The melt inclusions were analyzed using a 15 kV
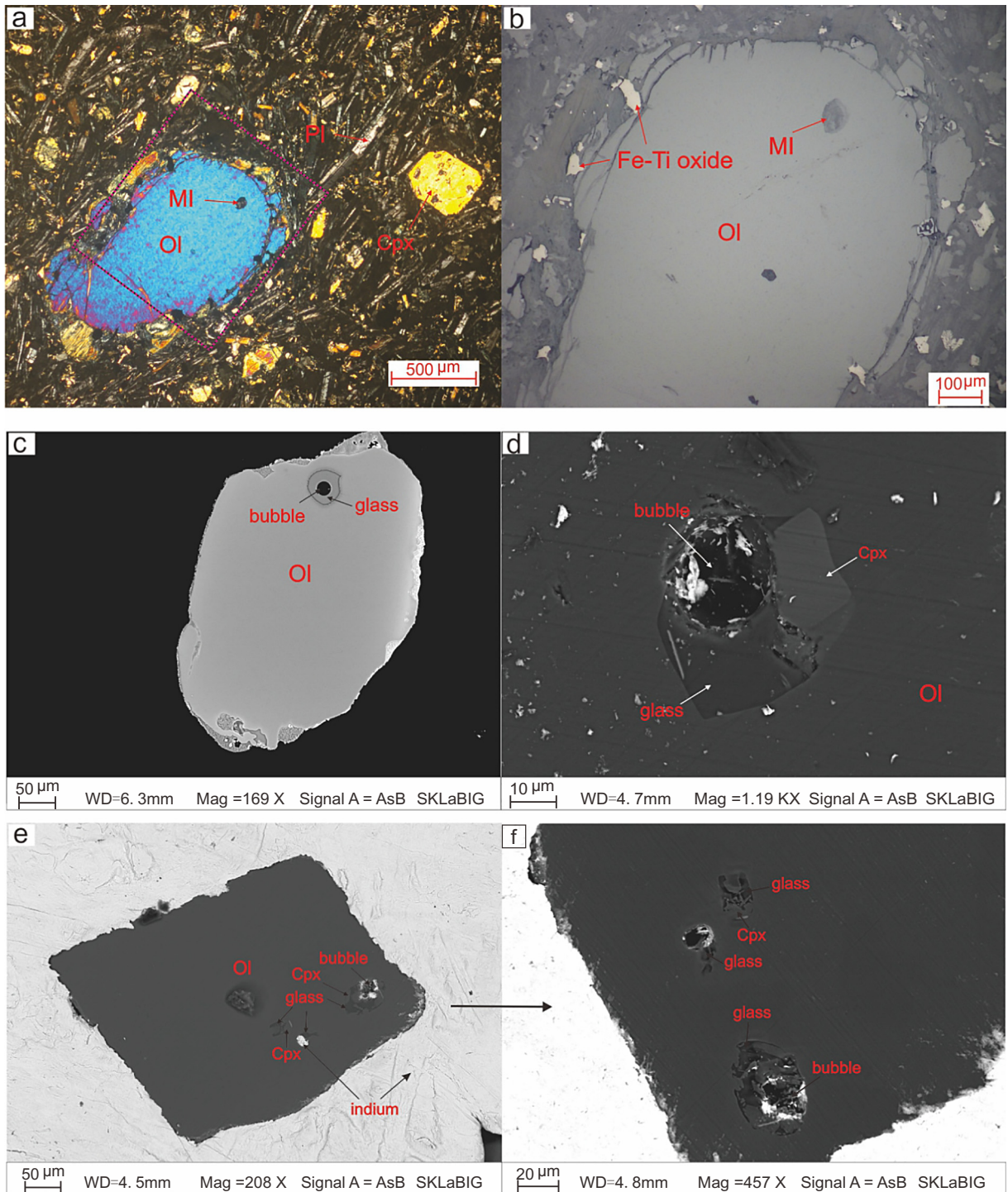
Fig. 2. Petrography of the Antang basalts and the melt inclusions in olivine. (a) Photomicrograph of olivine basalt under crossed polarized light. (b) Olivine phenocryst in (a) highlighting melt inclusion under reflected light. (c) A homogenized melt inclusion in olivine. (d) and (e) Original (unhomogenized) melt inclusions in olivine. (f) Enlarged melt inclusion shown in (e). Abbreviations: Ol: olivine; Cpx: clinopyroxene; MI: melt inclusion; Pl: plagioclase.

accelerating voltage, 200 nA beam current and 3 μm beam diameter. The volatile elements (Na, K) were analyzed with peak counting time of 10 s and background counting time of 5 s. Repeated analyses on the internal glass standard (JB-2) showed that the analytical uncertainty was less than 2% for SiO_2, Al_2O_3, FeO and CaO, and ~5% for TiO_2, MgO, Na_2O and K_2O (Table S1b).

The trace element composition of the melt inclusions was analysed by a CAMECA HR-SIMS-1280 ion microprobe at GIGCAS, using a 10 nA, −13kv primary beam of O_2^- ions and detection of positive secondary ions with a nominal acceleration voltage of + 10 kV. The target area on the sample was pre-sputtered for 100 s using a 25 μm × 25 μm rastering technique to remove the gold coat. During the analysis, the contrast aperture of 400 μm and the field aperture of 5000 μm×5000 μm were used. The magnification of the transfer system was configured as ~100 (equivalent to 80 μm). The entrance slit and the exit slit was set at ~200 μm and 600 μm, respectively. The energy window was 50 eV and 5 eV energy gap. Energy filter was employed −55 V for most elements except for Rb and Pb (−75 V), and Er and Yb (−65 V). Each analysis consisted of a 10-cycle running time and the following isotopes were analysed: ^{28}Si, ^{30}Si, ^{85}Rb, ^{88}Sr, ^{89}Y, ^{90}Zr, ^{93}Nb,

^{138}Ba, ^{139}La, ^{140}Ce, ^{141}Pr, ^{143}Nd, ^{149}Sm, ^{157}Gd, ^{165}Ho, ^{167}Er, ^{172}Yb, ^{208}Pb, ^{232}Th, and ^{238}U. A single analysis normally took 20 minutes. The trace element concentrations of melt inclusions were normalized to ^{28}Si, which had already been measured by EPMA. Rb, Sr, Y, Zr, Nb, Ba, La, Ce, and Nd calibrations were performed using the values obtained by repeated analyses of standards BHVO-2G, BCR-2G, BIR-1G GSD-1G, and GSC-1G. Pr, Sm, Gd, Ho, Er, Yb, Pb, Th, and U calibrations were performed using those analyzed values of standards BHVO-2G, BCR-2G, BIR-1G, and GSC-1G. Repeated analyses of the monitor glass standard (TB-1G) showed that the analytical errors were usually less than 15%, except for Th, U and Pb (~25%) (Table S1c).

3.5. Major element analyses of glass and mineral in unhomogenized melt inclusion (UMI)

Major elements of glass and mineral in UMI were determined by a Shimadzu Electron Probe Microanalyzer EPMA-1720 at Sun Yat-Sen University. The analytical conditions are 15 kV accelerating voltage, 20 nA beam current and 3 μm beam diameter. The JB-2 was used as the internal standard for the glass analysis. Repeated analyses on the internal glass standard showed that the analytical uncertainty was less than 2% for SiO_2, FeO, CaO and K_2O, and 5% for TiO_2, Al_2O_3, MgO and Na_2O.

3.6. H_2O content and H isotope analyses of UMI

Previous studies of olivine-hosted melt inclusions showed that loss of hydrogen occurred during laboratory heating of the host olivine, which could also lead to a decrease of the H_2O content and an increase in the hydrogen isotope composition of the melt inclusions (Chen et al., 2011; Gaetani et al., 2012). Thus, the H_2O and H isotope analyses in this study were performed on the original melt inclusion without homogenization.

During sample preparation, the olivine grains were embedded in Crystal-bond resin to avoid the contamination of epoxy in cracks. They were ground and polished on one side until the melt inclusions were exposed. Then the olivine grains were cleaned in acetone in an ultrasonic bath to remove Crystal-bond resin. The resin-free polished olivine grains were set into indium disks. After coating with gold, the samples were loaded and stored in the vessel chamber of a Nano-SIMS 50L for three days. The chamber was maintained at high vacuum ($< 5 \times 10^{-10}$ torr) during the analytical session. More detailed descriptions of the sample preparation are reported in Hu et al. (2015).

The hydrogen isotopic compositions and water content were measured with a Cameca Nano-SIMS 50L at the Institute of Geology and Geophysics, Chinese Academy of Sciences. Each 10 μm ×10 μm analyses area was rastered by a Cs^+ beam of ~0.5 nA and a diameter of ~5 μm. An electron gun was applied for sample surface charge compensation, which maintains an electron cloud over the area of analysis. Each analytical site was pre-sputtered for 2 min by rastering a 10 μm ×10 μm with a beam current of 2 nA to eliminate surface contamination and achieve stable yield rates of the secondary ions. A mass resolving power (MRP) of 1800–2000 (M/ΔM, Cameca definition related to the width between 10% and 90% intensity of the peak) is sufficient to resolve $^2D^-$ from the interference of $^1H_2^-$ and $^{18}O^-$. Each analysis contained 20 blocks of 20 cycles with a total counting time of ~3 min, and the ions were collected with electron multipliers. The detailed analytical procedure is described in Hu et al. (2015, 2019).

During the analyses, the instrumental mass fractionation (IMF), matrix effect and water concentration calibration curves were made by analyzing two apatite reference materials, Durango apatite (0.0478 wt% H_2O) and Kovdor apatite (0.98 ± 0.07 wt% H_2O and δD = −66 ± 21‰), and one MORB glass reference material SWIFT MORB glass (0.258 wt% H_2O). Previous water and H isotope analyses have showed similar matrix effects for silicates with a range from basaltic to rhyolitic composition, and there were no observable difference of matrix and IMF effects in both apatite and silicate glasses by NanoSIMS (Hu et al., 2015, 2019). The H isotope compositions were calibrated for instrumental

mass fractionation (IMF), using $\alpha_{IMF} = (D/H_{measured})/(D/H_{recommended})$. The hydrogen isotopes are presented in the form of $\delta D = ((D/H)_{sample}/(D/H)_{SMOW} - 1) \times 1000‰$, where SMOW is the standard mean ocean water with a D/H ratio of 1.5576×10^{-4} (McKeegan et al., 2006). The water content was determined from the $^1H^-$ intensities relative to $^{18}O^-$ using the calibration curves of $[^1H/^{18}O] = \alpha \times [H_2O] + \beta$. Repeated analysis of those standards give $[^1H/^{18}O] = 1.0039 \times [H_2O]$, $R^2 = 0.9944$, and $\alpha_{IMF} = 0.897 \pm 0.012$ (2σ) (Table S1d). One of the analytical errors is from the statistical uncertainty of the D/H ratios (most < 30‰ for δD) and $^1H/^{18}O$ ratios (<0.3 wt% for H_2O content). The other analytical error is ascribed to the uncertainties in α_{IMF} values and the slopes of the calibration curves. Thus, the reproducibility was monitored before and after each batch analysis through repeated measurements of the MORB glass (SWIFT) using the obtained α_{IMF} and the calibration curves. The measured water contents and H isotopic compositions of standard SWIFT are listed in Table S1e.

4. Results

### 4.1. Chemical and isotopic composition of the bulk rocks

The Antang basalts have an alkaline affinity and span a narrow whole-rock compositional range (Table S2), with SiO_2 = 46.4–46.8 wt%, MgO = 8.3–8.8 wt%, and CaO = 7.9–8.3 wt%. Their mantle-normalized trace element patterns show enrichments in Nb-Ta, depletion of fluid-mobile (e.g., Rb, K and Pb), and heavy rare earth elements (HREEs), analogous to typical HIMU basalts from St. Helena (e.g., Hanyu et al., 2011; Kogiso et al., 1997a; Weaver, 1991) (Fig. 3). These rocks also display unradiogenic Sr ($^{87}Sr/^{86}Sr(i)$ = 0.7032–0.7040), moderately radiogenic Nd ($^{143}Nd/^{144}Nd(t)$ ~ 0.5127), Hf ($^{176}Hf/^{177}Hf(t)$ ~ 0.2830), and Os ($^{187}Os/^{188}Os(t)$ = 0.1653–0.2740), and highly radiogenic Pb isotopic compositions, e.g., $^{206}Pb/^{204}Pb$ = 19.17–19.44, $^{207}Pb/^{204}Pb$ = 15.55–15.59 and $^{208}Pb/^{204}Pb$ = 39.29–39.56 (Table S2; Fig. 5).

4.2. Chemical and O isotopic compositions of olivine

The olivine phenocrysts span a range of forsterite (Fo) compositions between 77.9 and 85.9. They have lower CaO contents (0.07–0.26 wt%, Table S3) than olivines from MORBs and carbonated peridotite-derived basalts, and most have CaO contents lower than olivine in the plume-related Hawaii basalts (Fig. 6a). The morphologies, textures, and compositions of olivine and the presence of melt inclusions strongly support a magmatic origin for the olivine phenocrysts. Most of olivines yield mantle-like oxygen isotope compositions, with a $\delta^{18}O$ range of 5.04–5.50‰, except for some olivines with $Fo_{82.0-85.9}$ showing slightly higher $\delta^{18}O$ values up to 6.01‰ (Table S3; Fig. 6b).

4.3. Composition of HMI and estimated primary magma

Olivine-hosted melt inclusions may re-equilibrate with their host olivine by Fe-Mg exchange reaction (Danyushevsky et al., 2000). This re-equilibrium process is generally called "Fe-loss" and usually results in an increase of MgO and a decrease of FeO^T (total iron oxides, Danyushevsky et al., 2000). The negative correlation between FeO content of the melt inclusions and Fo of the host olivine indicates that there was Fe-Mg exchange between them (Fig. S1). Furthermore, the nearly constant CaO/Al_2O_3 ratio follows the range of Fo of olivine between 82.2 and 85.9, suggesting only olivine fractionation during magmatic differentiation (Fig. 4). We thus use the PETROLOG software (Danyushevsky and Plechov, 2011) to adjust the measured melt inclusion compositions using the "Fe-loss" correction so that we can obtain the composition of the melt in equilibrium with the host olivine. This calculation requires an independent estimation of the initial trapped melt FeO^T content. According to the FeO^T fractionation trend, 10 wt% is set as the FeO^T content in the initially trapped melt (Table S4a; Fig. S1). After applying the "Fe-loss" correction, the homogenized melt
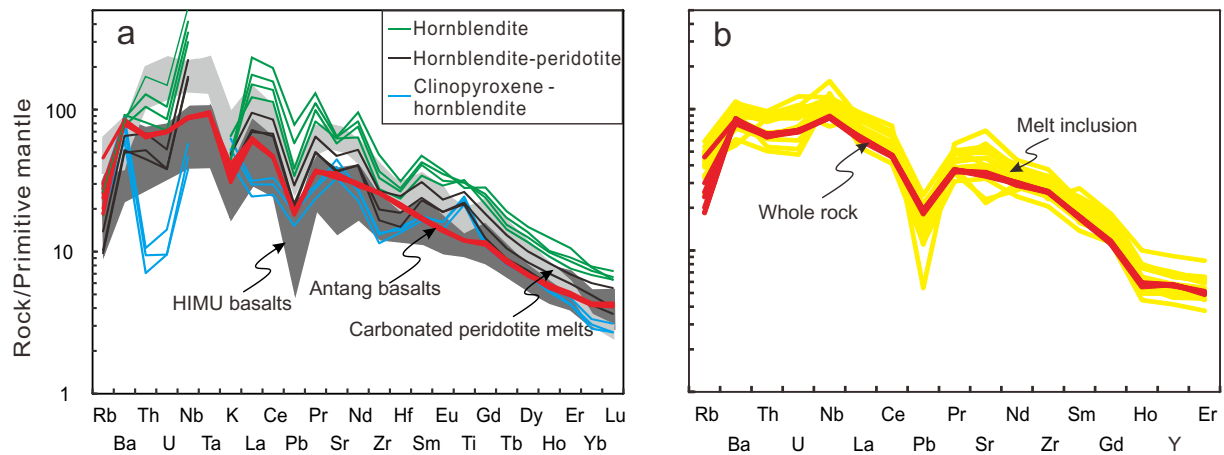
Fig. 3. Primitive mantle-normalized trace element spidergram of bulk rocks (red lines in both a and b) and melt inclusions (yellow lines in b) of the Antang basalts, and the melts derived from carbonated peridotite (Zeng et al., 2010), hornblendite, clinopyroxene-hornblendite, and hornblendite-peridotite (Pilet et al., 2008). HIMU basalts from St. Helena (Kawabata et al., 2011) are also plotted for comparison. Normalized values for primitive mantle are from Sun and McDonough (1989).

inclusions in olivine show a range in SiO_2 of 44.6–47.3 wt%, in MgO of 6.6–8.3 wt% and in CaO of 8.8–10.7 wt% (Table S4b). The whole-rock chemical composition can be roughly estimated as 93–96% melt inclusion plus 4–7% olivine, consistent with the dominance of olivine phenocrysts in the basalt.

In the case of unique olivine fractionation, the primary magma composition of basalts can be calculated through addition of olivine back into the melt until chemical equilibrium between the estimated primary magma and mantle olivine is reached. We therefore selected those melt inclusions within high-Fo (>82.2) olivine to estimate the primary magma composition of the Antang basalts through addition of olivine in 0.1% increments (assuming that 10% of the total iron is Fe^{3+} and $(Fe^{2+}/Mg)_{olivine}/(Fe^{2+}/Mg)_{melt} = 0.3$). The melt compositions are corrected so that they are in equilibrium with an olivine composition of Fo_{90}. The estimated primary magmas span a SiO_2 range of 44.3–46.1 wt%, a MgO range of 13.8–14.4 wt%, and a CaO range of 7.3–8.7 wt% (Table S4c), which can be reconstructed by adding 14–19% olivine back into 81–86% corrected melt inclusion. The magmas also have low CaO contents compared with the experimental melts of peridotite, but show similar CaO contents to melts of eclogitic or pyroxenitic sources (Fig. 7).

The melt inclusions also show similar trace element patterns to the bulk rocks, confirming the HIMU-like feature of Antang basalts (Table S5; Fig. 3b).

magma mixing, and surface weathering or alteration. The absence of secondary minerals (Fig. 2a) suggests an insignificant effect of alteration on the Antang basalts. However, the whole-rock composition may be easily affected by the surface alteration, especially for fluid-mobile elements such as K, Rb, Ba, and Sr. As shown in Fig. 3 and Table S2, except for the sample JA16-14 showing a fluctuating Rb, the other incompatible elements show consistent trace element patterns. This suggests that surface alteration should be negligible for the most of the Antang basalts.

The Mesozoic Antang basalts and their olivine-hosted melt inclusions have high Nb/U and Ce/Pb ratios and show positive Nb-Ta anomalies and prominent Rb, K and Pb depletion (Fig. 3), indicating a negligible role for crustal contamination or assimilation. The relatively homogeneous compositions of the olivine-hosted melt inclusions also preclude any significant magma mixing in their generation.

Fractional crystallization of mantle-derived primary melts during magmatic evolution would significantly change the chemical composition of the melts. The Antang basalts show lower Mg# (65.4−66.7) than those of typical mantle-derived primary melts (Mg# = 73−81), implying a role of fractional crystallization. Melt inclusions are small portions of magma trapped by growing crystals and represent snapshots of the crystallization environment (Danyushevsky et al., 2000). The correlation between Fo of the host olivine and CaO/Al_2O_3 ratios of

4.4. Composition, water content and H isotope ratio of UMI

Glasses in UMI show a range in SiO_2 of 56.2–62.9 wt%, in Al_2O_3 of 17.4–23.6 wt%, in CaO of 1.11–5.04 wt%, and K_2O of 1.34–4.16 wt% (Table S7). The recrystallized mineral in the UMI belongs to augite, spanning a SiO_2 range of 40.9–42.8 wt%, an Al_2O_3 range of 13.55–15.59 wt%, a FeO range of 6.70–9.38 wt%, a MgO range of 9.23–12.66 wt%, and a CaO range of 12.11–23.49 wt% (Table S7).

The UMI spans a large range in H_2O from 0.34 to 4.97 wt% and a δD range between -102 and 141‰ (Table S6). The H_2O content shows a broadly negative correlation with δD (Fig. 8a). The melt inclusion hosted in olivine with Fo number less than 82 has a relatively low H_2O content and δD value (Fig. 8b).
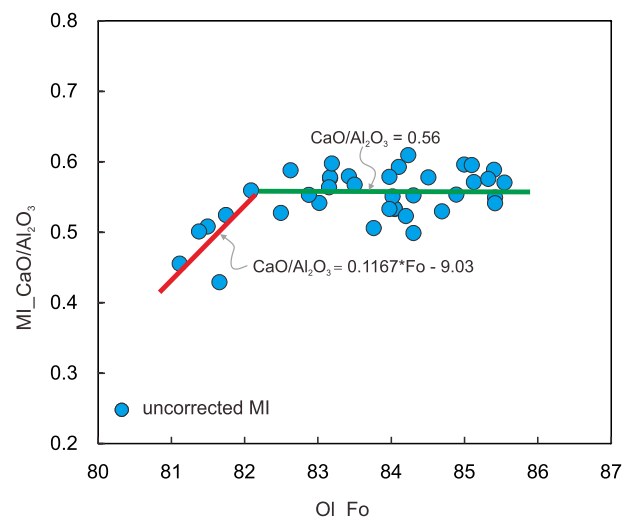
5. Discussion

5.1. Effects of alteration, crustal assimilation, and fractional crystallization

Basaltic rocks can undergo open-system compositional evolution through processes such as crustal contamination or assimilation,

Fig. 4. The CaO/Al_2O_3 value of melt inclusion versus the Fo number of host olivines.

the melt inclusions indicates that clinopyroxene fractionation took place at Fo < 82.2 (Fig. 4). Moreover, the lack of Sr and Eu anomalies (Fig. 3a) implies that fractional crystallization of plagioclase was negligible during the formation of Antang basalts. In summary, the geochemical features of whole-rock and melt inclusion indicate the Antang basalts mainly experienced a role of olivine + clinopyroxene fractionation, whereas the effect of alteration and crustal assimilation could be negligible.

5.2. Effects of magmatic evolution and post-entrapment processes on H₂O content of melt inclusion

Since H_2O is more readily exchanged than most incompatible elements during magmatic evolution and post-entrapment processes, it is important to assess whether the magmatic H_2O concentrations of the melt inclusions have been compromised by exotic fluid addition, magma degassing, and post-entrapment diffusion and crystallization (e.g., Chen et al., 2011; Gaetani et al., 2012).

Most of olivine phenocrysts have mantle-like $\delta^{18}O$ values (Fig. 6b), confirming the negligible influence of low-temperature alteration. Any addition of meteoric water or seawater with high δD should produce a positive correlation between H_2O and δD, which is opposite to the negative correlation in the UMI (Fig. 8a). Aqueous fluid addition will significantly change concentrations of fluid-mobile elements of olivine-hosted melt inclusions (Kogiso et al., 1997b).

However, the melt inclusions in the Antang basalts show low Rb/Nb, Ba/Nb, and Sr/Nb ratios and positive correlations of Zr with Rb, Ba, Th, and U, precluding the possibility of extra fluid addition during olivine crystallization (Fig. 9).

Although we analysed the water content of UMI to avoid water loss during the heating and homogenization processes, the loss of water (or H diffusion) may also have occurred during eruption and cooling of the magma (e.g., Gaetani et al., 2012; Saal et al., 2002). During magma ascent, the solubility of water in magma is mainly controlled by pressure and may reach the critical point at shallow depths. Magmatic degassing will reduce both the water content and δD. The melt inclusion hosted in olivine with Fo number ranging from 82 and 86 exhibits a negative correlation between H_2O and δD, which is contrary to the effect of magmatic degassing (Fig. 8a). However, the UMIs hosted in olivine with Fo < 82 show a dramatical decrease of H_2O and δD ratio, which could be affected by degassing (Fig. 8).

After entrapment in the host olivine, the H_2O content of melt inclusion may decrease via hydrogen diffusion through olivine to keep dynamic equilibrium with the residual magmas (Chen et al., 2011). It is nearly impossible to avoid diffusive loss of hydrogen during magma ascent, because the timescale of magma ascent is close to that of diffusive water exchange as experimentally determined (Gaetani et al., 2012; Hauri, 2002). Since the diffusion of H is much faster than D, hydrogen diffusion through host olivine will lead to an increase of δD in association with a decrease of H_2O content in melt inclusion. A large number of UMIs from the Antang basalts have fairly positive δD values, which were probably a result of post-entrapment kinetic diffusion (Fig. 8a). By contrast, the UMI with the highest water content (up to 5.0 wt%) and mantle-like δD value experienced insignificant hydrogen diffusion.

Crystallization of daughter mineral in melt inclusion will lead to an increase of water content in the residual glass. This process does not reset δD value of the residual glass. The petrographic examination (Fig. 2) shows that the water content of glass in the UMI cannot represent the primary water content of the melt trapped by host olivine, because of the crystallization of daughter mineral. In this respect, it is necessary to reconstruct the water content of primary melt by analysing the relative volume of glass and recrystallizing mineral within the UMI.

The recrystallized mineral in the UMI belongs to augite, which would dramatically decrease the CaO/Al_2O_3 ratio of residual glass. Because the CaO/Al_2O_3 ratio of melt inclusion shows a good correlation with Fo number of host olivine (Fig. 4), we calculate the proportion of

glass and mineral using the analysed CaO/Al_2O_3 ratios of glass and mineral in the UMI and the variation trends of CaO/Al_2O_3 of HMI at given Fo component of host olivine. With the following equation, we calculate the proportion of glass and mineral within each UMI:

$$CaO/Al_2O_3\ (HMI) = a \times CaO/Al_2O_3\ (glass\ in\ UMI) + b \\ \times CaO/Al_2O_3\ (mineral\ in\ UMI)$$

Where $a + b = 1$

$$CaO/Al_2O_3\ (HMI) = 0.56\ (When\ the\ host\ olivine\ has\ Fo > 82.2, Fig. 4)$$

$$CaO/Al_2O_3\ (HMI) = 0.1167 \\ \times Fo–9.03\ (When\ the\ host\ olivine\ has\ Fo < 82.2, Fig. 4)$$

The results yield that the proportions of post-entrapment crystallization in these UMIs span a range from 16 to 58% (Table S7). The melt inclusion with the highest water content (4.97 wt%) and low δD experiences ~34% post-entrapment crystallization, yielding 3.28 wt% H_2O for the bulk UMI, which should represent the minimum of its water content. Considering that the Antang basalts might have experienced about 14–19% olivine fractionation, we finally estimate that the primary magma of Antang basalts was hydrous with at least 2.65 wt% H_2O.

5.3. Petrogenesis of the Antang basalts

The HIMU-like whole-rock geochemistry and the H_2O-rich compositions indicate derivation of the Antang basalts from a hydrous mantle reservoir. Possible mantle sources for HIMU-like basalts include metasomatized lithospheric mantle (hornblendite, hornblende-bearing mantle and carbonated peridotite) (e.g., Pilet et al., 2008; Weiss et al., 2016) and ancient recycled oceanic crust (e.g., Hanyu et al., 2011; Hofmann, 1997). However, the low TiO_2, high SiO_2, MgO and FeO contents and the lack of negative Zr-Hf anomalies distinguish the Antang basalts from melts of hornblendite or hornblende peridotite (Fig. 3). In addition, the contemporaneous HIMU-like Ningyuan basalts, which intrude the Cathaysia Block around 300 km to the southwest (Wang et al., 2008) (Fig. 1), contain Mesozoic mantle xenoliths that are characterized by the lack of hydrous minerals, nearly flat REE patterns, and depletion of Ba (Zhang et al., 2008). These features of xenoliths imply that the lithospheric mantle beneath South China was nearly anhydrous with little metasomatism from subducted slab-derived fluids. Furthermore, the relatively low Os concentrations and high $^{187}Os/^{188}Os(t)$ ratios of the Antang basalts (Fig. 10a, b) are inconsistent with melts derived from sub-continental lithospheric mantle (SCLM), which typically has extremely high Os concentrations and low $^{187}Os/^{188}Os$ ratios. The mantle peridotite xenoliths hosted in Jurassic Ningyuan basalts have higher Sr ($^{87}Sr/^{86}Sr(i) = 0.7048–0.7050$) and lower Os ($^{187}Os/^{188}Os(t) = 0.1206–0.1293$) isotopic ratios than those of the Antang basalts (Liu et al., 2012; Zhang et al., 2008) (Fig. 10c). If the Antang basalts were derived from the same source as the mantle xenoliths, this could have required a large (>90%) continental crustal input to match the Os-isotopic ratios of the primitive Antang magmas (Fig. 10d). This is inconsistent with the HIMU-like trace element features of the Antang basalts that permit negligible crustal contamination. We therefore conclude that the geochemical data from the Antang basalts argue against derivation from the SCLM regardless of whether or not it experienced metasomatism.

A systematic study on the primary magmas has revealed that pyroxenite is the principal lithology in the mantle source of Late Mesozoic basalts in SE China (Zeng et al., 2016). Following the method in Thompson et al. (2005), the calculated primary melts were plotted on the CIPW normative Di-Ol-Hy-(Ne+Lc)-Qz projection, along with experimentally determined mantle-derived melts from peridotite, carbonated peridotite, carbonated eclogite, hornblendite, clinopyroxene-hornblendite, silica-deficient pyroxenite and silica-excess pyroxenite (Fig. 11). The

Antang basalts plot within the compositional range of silica-deficient garnet-pyroxenite melts. Because clinopyroxene is typically the major CaO-bearing mantle phase, leaving clinopyroxene as a major residual phase is the only effective way of lowering the CaO content of mantle-derived melts (Herzberg, 2011). The low CaO contents (7.3–8.7 wt%) of the primary magmas (Fig. 7) also support a pyroxenitic residue rather than a peridotitic residue in the mantle source. Moreover, the Antang basalts define a negative correlation of Th versus Nb/Ta and Nb/La (Fig. S2), implying a bulk $D_{Nb/Ta} > 1$ and $D_{Nb/La} > 1$. This is a typical characteristic of an eclogitic source because $D_{Nb/Ta}$ and $D_{Nb/La}$ for eclogitic garnet range from 1.2 to 2.0 and 1.3 to 7.5 (e.g.,Klemme et al., 2002 ; Pertermann et al., 2004), respectively. Partition coefficients show that $D_{Zr} < D_{Hf}$ in clinopyroxene and $D_{Zr} > D_{Hf}$ in garnet (Klemme et al., 2002; Pertermann et al., 2004). Thus, low degree melting of a clinopyroxene-rich eclogite can explain the elevated Zr/Hf ratios (43–45) of the Antang basalts. The low CaO content of olivine (Fig. 6a) further indicates a pyroxenitic source (Sobolev et al., 2007). In summary, the residual source region for the Antang basalts was dominated by clinopyroxene and garnet.

Recycled upper oceanic mafic crust is known to form eclogitic or pyroxenitic mantle reservoirs (e.g., Kogiso and Hirschmann, 2006; Sobolev et al., 2007). Extremely high $^{187}Re/^{188}Os$ ratios reported in oceanic crust (80 to 675) would lead to high radiogenic $^{187}Os/^{188}Os$ ratios over 1.0 Ga

(Peucker-Ehrenbrink et al., 2012). A major contribution from such a mantle source is also suggested by the relatively high whole-rock $^{187}Os/^{188}Os(t)$ ratios of the Antang basalts (Fig. 10) and the relatively high $\delta^{18}O$ values in high-Fo (>82) olivine (Fig. 6b). In order to further determine how the mantle source for the Antang basalts was formed, we compared their isotopic compositions with modelled Sr-Nd-Pb-Hf isotopic evolution paths for both ancient subducted oceanic crust and contemporary subducted sediment (Table S8, Stracke et al., 2003). Compared with typical HIMU basalts, the Antang basalts have lower $^{206}Pb/^{204}Pb$ and higher $^{87}Sr/^{86}Sr$ ratios (Fig. 5), and plot in the 1.0–1.5 Ga arrays defined by the mixing curves between contemporary subducted oceanic crust and sediments. These results further suggest that the Antang basalts were derived from a HIMU-like mantle reservoir composed principally of 1.0–1.5 Ga recycled oceanic crust plus minor (<1 %) sediment. The involvement of minor sediment may also contribute to the Ba enrichment observed in the Antang basalts (Fig. 3, Weaver, 1991).

5.4. Estimation of H₂O in the mantle source

Geochemically, H_2O behaves incompatibly during partial melting, with a partitioning coefficient similar to that of Ce (Michael, 1995); thus, the H_2O/Ce ratio of magma has been proven to be a useful
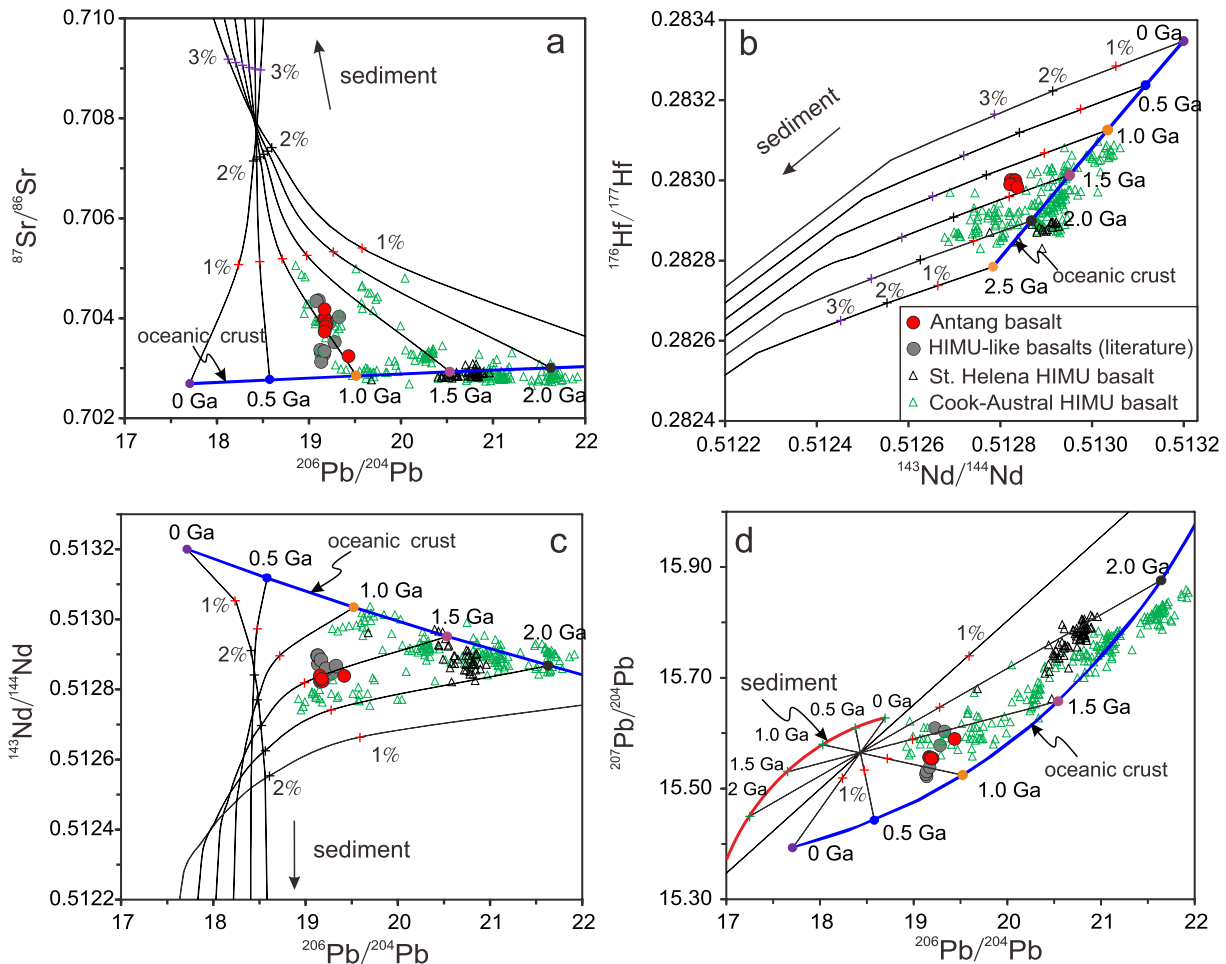
Fig. 5. Sr-Nd-Pb-Hf isotopic comparison between the Antang basalts and typical HIMU basalts, modelling the evolution of recycled oceanic crust plus contemporary sediment (Stracke et al., 2003). The solid blue line with solid circles shows the isotopic growth of recycled oceanic crust. The black lines with crosses connect the recycled oceanic crust and the subducted sediment of various ages (0–2.5 Ga). The numbers on the curves denote the mass fractions of sediment in the mixed source. The isotopic compositions of St. Helena and Cook-Austral HIMU basalts are compiled from the GEOROC Database (http://georoc.mpch-mainz.gwdg.de/georoc/). The typical HIMU basalts with $^{206}Pb/^{204}Pb > 20.5$ can be interpreted as melts from 2.0–1.5 Ga recycled oceanic crust, whereas those with $19.0 < ^{206}Pb/^{204}Pb < 20.5$ are related to younger recycled oceanic crust (1.0–1.5 Ga) and/or to the addition of minor sediment (0–1%) to the source. The isotopic composition of the Antang basalts indicates their derivation from a mantle source comprising mainly 1.0–1.5 Ga recycled oceanic crust plus minor sediment. The data for other HIMU-like basalts in SE China are from Wang et al. (2008). The detailed calculation process is presented in Table S8.
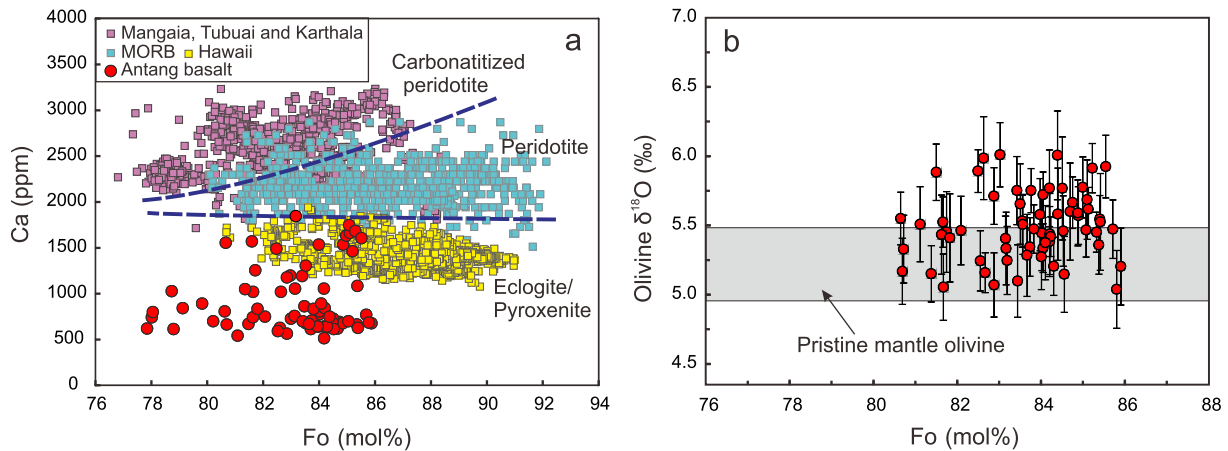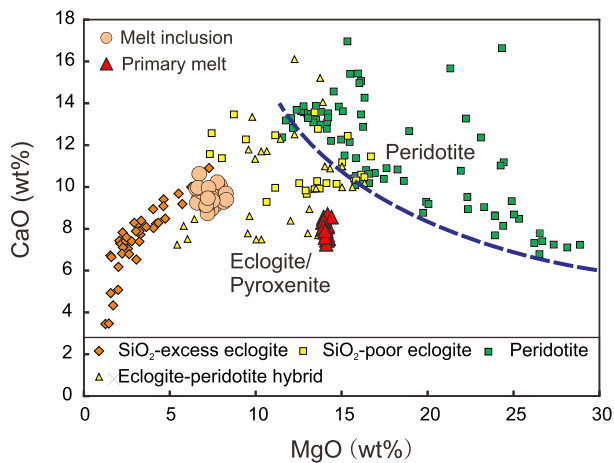
Fig. 6. (a) Ca (ppm) versus Fo (mol%) of olivine, showing the divisions (blue dashed lines) between carbonated peridotite, peridotite and eclogite/pyroxenite. The purple squares denote olivines of the basalts from Mangaia and Tubuai that were derived from carbonated peridotitic source (Weiss et al., 2016). The olivine data for MORB and Hawaii are compiled from Sobolev et al. (2007). (b) Plot of $\delta^{18}O$ versus Fo of olivine for the Antang basalts. The shaded band denotes the range of normal mantle olivine with $\delta^{18}O$ between 4.8 and 5.4‰ (Mattey et al., 1994).

geochemical tool to trace the hydrous state of mantle source (Dixon et al., 2002; Xia et al., 2019). Considering the Ce concentrations of the HIMI between 73 and 135 ppm and the primary H_2O content of melt inclusion is ≥3.28 wt%, the calculated H_2O/Ce ratios (243–450) of the Antang basalts are higher than MORB (100–200, Michael, 1995; Saal et al., 2002) and EM-type OIB (<150, Dixon et al., 2002), implying a hydrous mantle source.

In addition, the water content of the mantle source can be calculated at a given degree of melting and the hydrogen partition coefficient. Using an inferred eclogitic/pyroxenitic source, we then calculate the degree of partial melting based on the relationship between incompatible elemental ratios (e.g., La/Yb versus Sm/Yb). As the La, Sm, and Yb concentrations of the average depleted mantle (0.192 ppm, 0.239 ppm, and 0.365 ppm, respectively) are much less than that of mafic oceanic crust (~3.83 ppm, ~3.11 ppm, and ~3.03 ppm, respectively) (Stracke et al., 2003), some contribution of mantle peridotite could not greatly change the incompatible elemental ratios. To simplify the modelling, we use the elemental ratios of recycled oceanic crust as the starting component to calculate the degree of melting based on the relationship between incompatible elemental ratios (Sm/Yb versus La/La and La/Yb versus La/Sm). The recycled oceanic crust is assumed to consist of 99% mafic oceanic crust (25% N-MORB + 25% altered MORB + 50% gabbro)
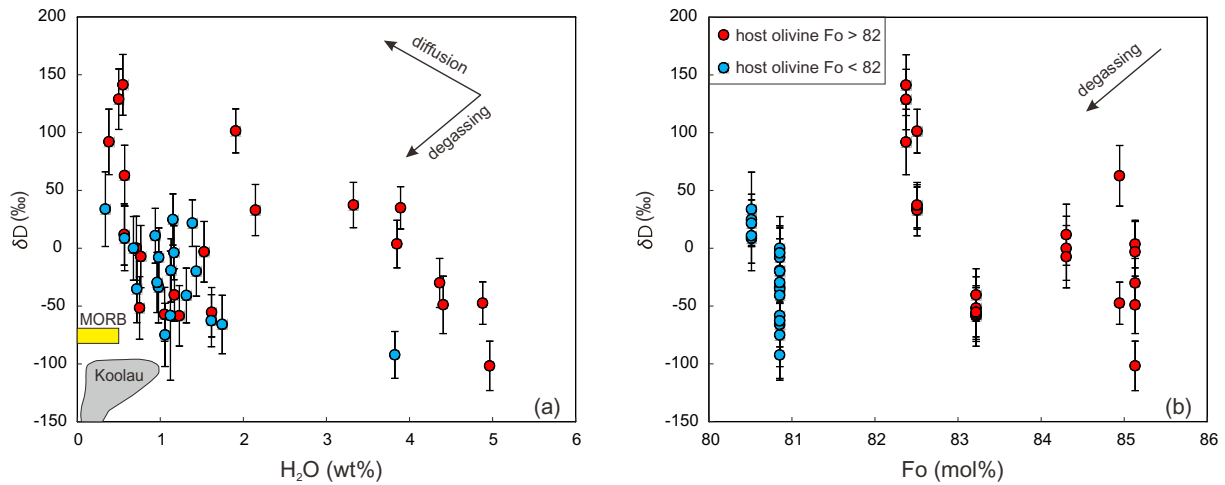
and 1% subducted sediment represented by global subducted sediment (GLOSS) (Reference can be seen in supplementary A1). Equilibrium non-modal melting calculation indicates that 4.5–6.0% melting of the assumed source can produce melts with the Antang basalt compositions (Fig. 12).

Previous SIMS analyses on H in nominally anhydrous minerals have facilitated direct determination of mineral/melt hydrogen partitioning from coexisting mantle minerals and hydrous silicate melts. A compilation of the published data over wide ranges of composition, temperature and pressure yields the range of $D_H^{Grt/liq}$ from 0.001 to 0.003 and a $D_H^{Cpx/liq}$ range from 0.01 to 0.03 (Hauri et al., 2006). The calculated bulk D_H value of eclogite with 80% clinopyroxene plus 20% garnet ranges from 0.008 to 0.024. In combination with the estimated primary magma that has H_2O ≥ 2.65 wt%, we finally estimate that the mantle source for the Antang basalts had H_2O contents between 0.14 and 0.22 wt%.

5.5. Origin from a hydrous MTZ

The lines of evidence from geochemical data of the bulk rock, olivine and melt inclusion from the Antang basalts suggest that the basaltic magmas were derived from a hydrous mantle source composed principally of eclogite/pyroxenite probably derived from an ancient recycled oceanic slab. The Sr-Nd-Pb-Hf isotopic composition of this hydrous HIMU-like mantle reservoir requires a long (1.0–1.5 Ga) mantle residence time and this requires at least two fundamental conditions: (1) long-term isolation from the convective mantle to avoid chemical and isotopic re-homogenization with the surrounding mantle, and (2) a relatively low temperature to avoid large-scale partial melting and isotopic disturbance. Considering the asthenosphere is dry (<200 ppm H_2O) (Saal et al., 2002) and the convection would make the recycled oceanic crust hard to be stagnated for a long time, these factors preclude the possibility that the Antang basalts were derived from the low-viscosity convective asthenosphere. Having already ruled out derivation from a metasomatized SCLM, the possible alternative sites include the MTZ, the lower mantle or the D″ layer (i.e. the core-mantle boundary).

Cold oceanic slabs can penetrate into the lower mantle and may bring a certain amount of water into the Earth's interior (Poli and Schmidt, 2002). The hydrous aluminosilicate phases, such as δ-AlOOH and Al-rich phase D and phase H can be stable under lower mantle conditions (Pamato et al., 2015). This suggests the possibility for the existence of locally hydrous sources within the lower mantle. However, the following arguments exclude the possibility that the Antang basalts were derived from the lower mantle: (1) Basalts associated with mantle plumes containing recycled subducted slabs are relatively dry

Fig. 7. CaO (wt%) versus MgO (wt%) plot of primary magmas to discriminate between (blue dashed line) the melts from peridotite and eclogite/pyroxenite. The primary magma compositions of the Antang basalts have been corrected for olivine fractionation (Table S4c). Data sources for melts of peridotite, SiO_2-excess eclogite, SiO_2-poor eclogite, and eclogite-peridotite hybrid are presented in "Supporting Information A1".

Fig. 8. (a) δD versus H₂O of the melt inclusions. The yellow band denotes the ranges for MORBs (Shaw et al., 2008). The range of Koolau melt inclusions is also shown for comparison (Hauri, 2002). (b) δD versus Fo of the host olivine.

(e.g., Dixon et al., 2002; Shaw et al., 2012). The geochemical features such as negative Pb anomalies (high U/Pb ratio or HIMU feature) of basalts that originate in the lower mantle also indicate the intense dehydration of such recycled subducted slabs (Kogiso et al., 1997a). The lower mantle is composed predominantly of Mg- and Ca-perovskite and ferropericlase and has low water storage capacity (< 200 ppm) (e.g., Bolfan-Casanova et al., 2002, 2003). Thus, the amount of water that can be transported into the lower mantle would be minor; (2) Some OIBs have originated from the lower mantle indeed have low water contents and δD values (Hauri, 2002), indicating that most of the lower mantle is relatively anhydrous; (3) Because the lower mantle is also convective (Chen, 2016), even if the cold subducted slab brings a certain amount of water into this region, any locally hydrous source will be rapidly homogenized. This means that it is difficult to form a long-term isolated hydrous source within the lower mantle.

Compared with the normal mantle, a deep (e.g., derivation from the D″ layer) mantle plume has an extremely high temperature. Based on

the estimated primary magma composition and the inferred hydrous eclogitic/pyroxenitic source of the Antang basalts, we calculate that the mantle potential temperature (Tp) spans a range of 1331–1386°C (Table S4d; Supporting Information A2). This Tp is similar to that estimated for the transition-zone derived hydrous mantle plume at Changbaishan (Kuritani et al., 2019). Also, there is no geological evidence to support that a mantle plume was active beneath South China during the Jurassic. Therefore, both the geological records and the estimated lower Tp at that time imply that the D″ layer cannot be the source of Antang basalts.

Alternatively, delamination and detachment of oceanic crust from the subducted slabs, with subsequent long-term storage in the MTZ quarantined from the effects of convective stirring, remains a viable option (Nebel et al., 2013; Ringwood, 1994). High-resolution tomographic images in modern subduction zones demonstrate that subducted slabs in some regions do not simply plunge directly through the 660 km discontinuity, deeply into the lower mantle (Kuritani et al., 2011, 2013,
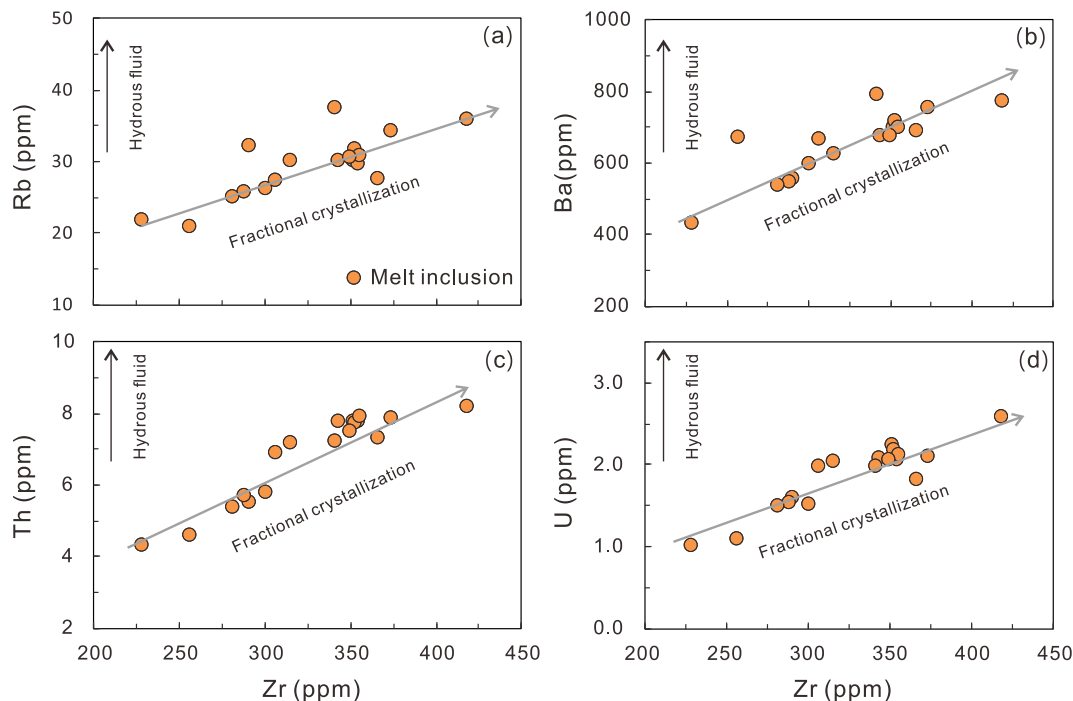

Fig. 9. Plots of (a) Rb vs. Zr, (b) Ba vs. Zr, (c) Th vs. Zr, and (d) U vs. Zr for the olivine-hosted melt inclusions.
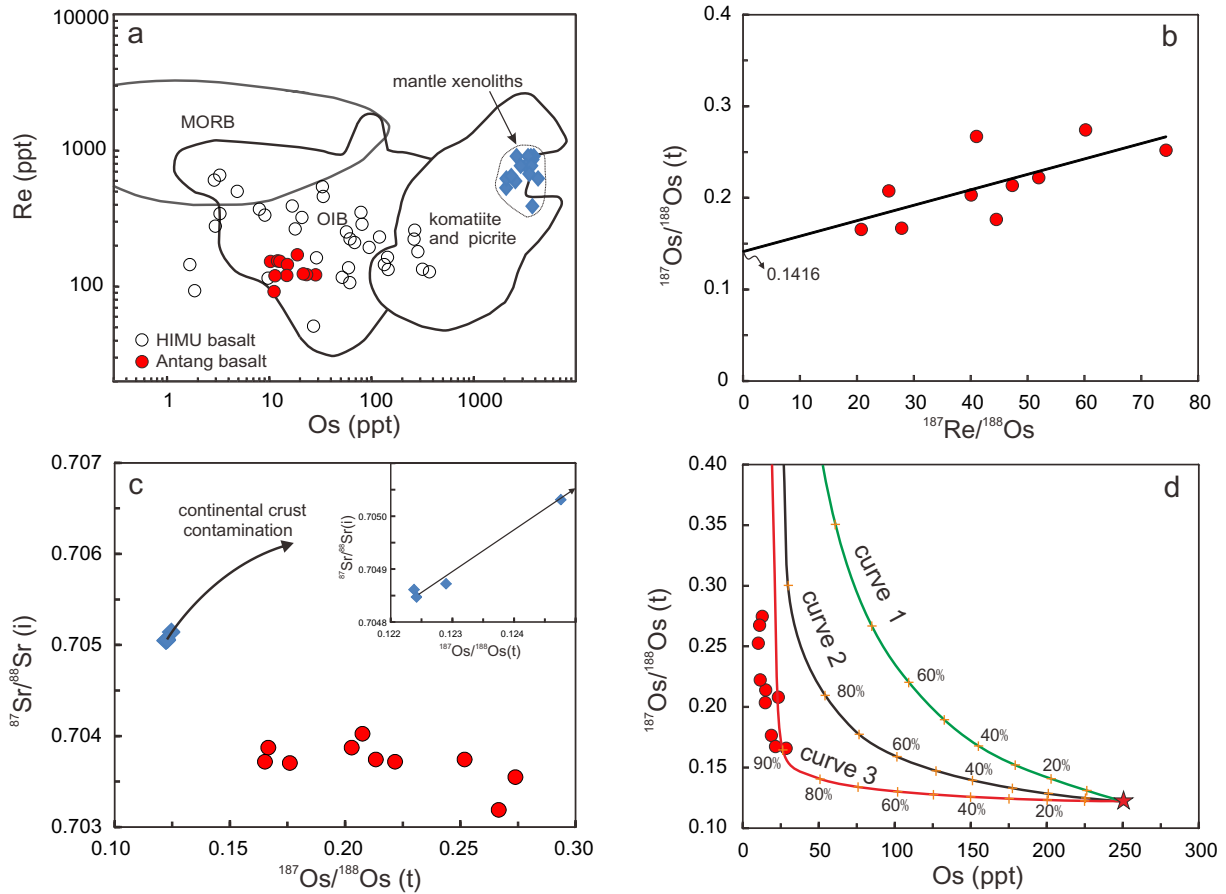
Fig. 10. Re-Os isotopic systematics of the Antang basalts. (a) Re versus Os compared with typical HIMU basalts from Cook-Austral (Hanyu et al., 2011) and mantle xenoliths (Liu et al., 2012; Zhang et al., 2008) from the contemporaneous Ningyuan basalts in South China. (b) The positive correlation between $^{187}Os/^{188}Os$ and $^{187}Re/^{188}Os$ indicates a nugget effect or disequilibrium binary mixing (Meibom et al., 2002). (c) $^{87}Sr/^{86}Sr(i)$ versus $^{187}Os/^{188}Os(t)$ for the Antang basalts and the mantle xenoliths. The broad negative correlation between $^{87}Sr/^{86}Sr(i)$ and $^{187}Os/^{188}Os(t)$ argues against a role for continental crust contamination. (d) The binary mixing lines (curves 1, 2 and 3) for melts derived from lithospheric mantle and crust. We assume that melts derived from lithospheric mantle have Os = 250 ppt and $^{187}Os/^{188}Os$ (168 Ma) = 0.1231, and that the continental crust has $^{187}Os/^{188}Os$ = 1.29 and an Os concentration of 15 ppt in curve 1, 5 ppt in curve 2 and 1 ppt in curve 3.

2019). The study of phase transformation in oceanic crust shows that the basaltic crust component would be 0.1-0.2 g/cm^3 lighter than its surrounding mantle pyrolite at the depths of 660–800 km (Irifune and Ringwood, 1993). The buoyancy produced by internal petrological differentiation may prevent basaltic crust entering the lower mantle and

segregate it to form a gravitationally stable layer overlying the 660 km discontinuity (Ringwood, 1994). The MTZ thus may contain recycled oceanic crustal components, at least partially shielded from mixing and petrological homogenization typical of the upper mantle. Therefore, the best interpretation is that the source of the Antang basalts was a
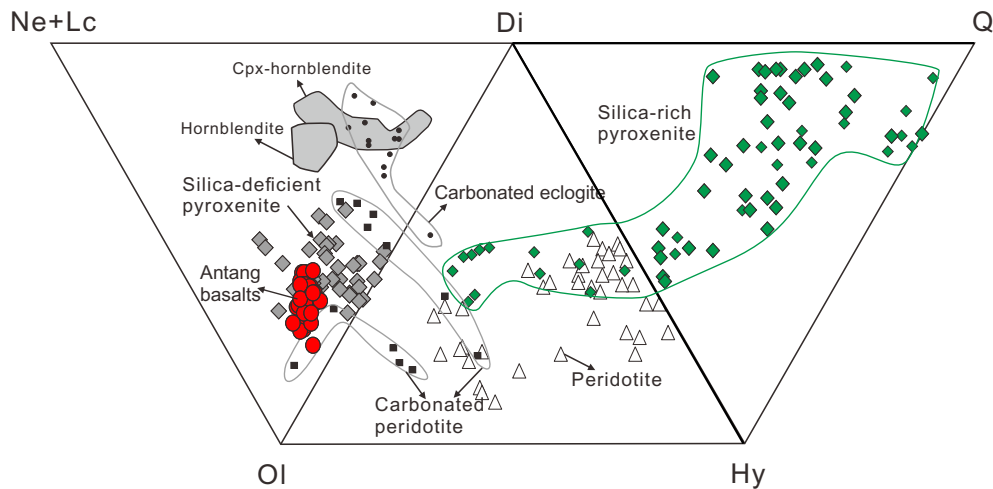
Fig. 11. CIPW normalization plotted in Ne + Lc (nepheline + leucitite), Ol (olivine), Di (diopside), Hy (hypersphene), Q (quartz) space (Thompson et al., 2005). Melt compositions in a range of partial melting experiments on various sources, including: hornblendite, cpx-hornblelndite, carbonated peridotite, carbonated eclogite, silica-deficient pyroxenite, silica-rich pyroxenite, and peridotite. All data were calculated using the assumption that 10% of the total iron as Fe_2O_3. The related references are listed in "Supporting Information A1".
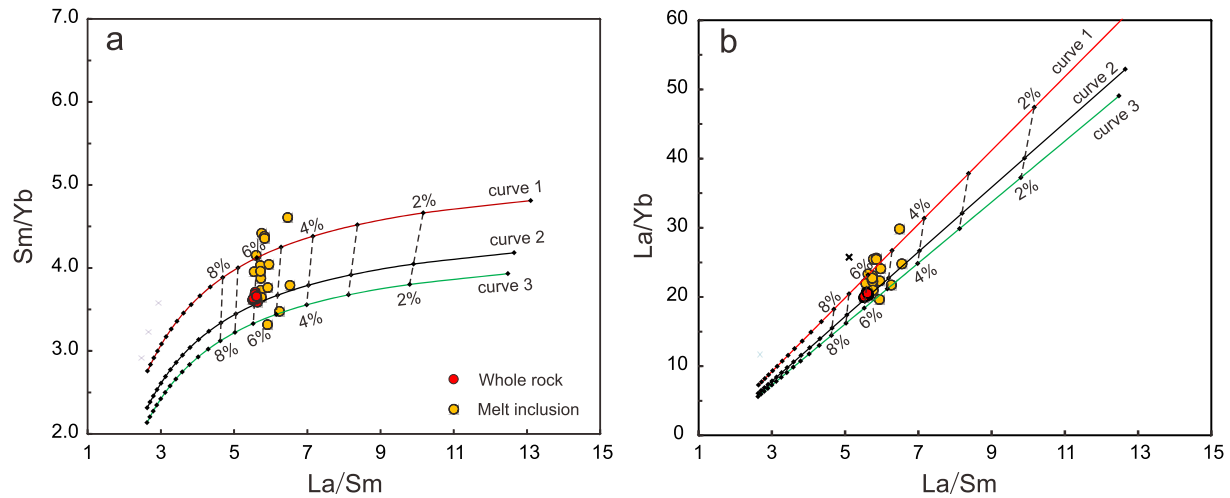
Fig. 12. La/Sm vs. Sm/Yb (a) and La/Yb (b) plots of the Antang basalts, modelling the melting degrees (F) of eclogite. During the calculation, the non-modal batch melting equation was used. The initial composition of the mantle source is assumed to comprise 99% basaltic oceanic crust (25% N-MORB + 25% altered MORB + 50% gabbro) and 1% subducted sediment represented by GLOSS, which has La = 3.88 ppm, Sm = 3.03 ppm, and Yb = 3.02 ppm. The residual assemblage of 75% Cpx + 25% Grt, 80% Cpx + 20% Grt and 82% Cpx + 18% Grt is assumed for Curves 1, 2 and 3, respectively. Numbers on the curves denote the degree of melting. Mineral abbreviations: Grt = garnet; Cpx = clinopyroxene. Data sources for the related parameters used in the calculation can be seen in "Supporting Information A1".

hydrous MTZ (0.14–0.22 wt% H_2O) beneath the South China interior. This hydrous MTZ was isolated from mantle convection for over one billion years.

The mechanism for upwelling of hydrous MTZ materials needs to be further discussed. The estimated mantle potential temperature argues against thermal buoyancy is a primary cause for the Antang basaltic magmatism. South China has been an active continental margin in association with subduction of the paleo-Pacific Ocean beneath the Eurasian Continent during Jurassic. Through 3-D numerical modelling, Faccenna et al. (2010) proposed that the focused mantle upwelling can be generated both ahead of slab in the back-arc region (the disturbing distance could be up to five times as that from trench to magmatic arc) and around the lateral edges of the slab. Moreover, hydrous mantle peridotite is lighter than dry mantle peridotite, so a wet focused mantle upwelling could be generated at the top of the MTZ (Kuritani et al., 2019; Wang et al., 2016). Generation of the Antang basalts might be ascribed to the co-effect of slab subduction and hydrous mantle source that led to passive upwelling of hydrous MTZ materials in South China interior.

5.6. Implications for intraplate magmatism

Subducted slabs in the present-day mantle display a wide variation in behaviour, where some slabs penetrate into the lower mantle, for example beneath Peru, the Marianas and Central America, whereas others seem to stagnate in the transition zone, for example beneath the Izu-Bonin region, South-Kurile and Japan (Agrusta et al., 2017). While mantle heterogeneity may be partly ascribed to internal mantle differentiation induced by partial melting and melt transport, the recycled subducted components buried at the core-mantle boundary have been widely accepted to form chemically heterogeneous reservoirs in the Earth (Hofmann, 1997). Regions of buoyant upwelling mantle plume are considered to return some of this ancient oceanic crustal material to the shallow mantle, where it melts to form compositionally variable OIBs (Hofmann, 1997). However, many intraplate OIB-type basalts form in splash, edge, or baby plumes, with the lack of features characteristic of plume-related magmatism, and therefore cannot be attributed to upwelling mantle plumes (Conrad et al., 2011). The compositional variation of these basalts may thus need further explanation. Recently, several studies have proposed that the MTZ may be a potential source for the generation of intraplate magmatism. Murphy et al. (2002) proposed that subducted sediment sequestered in the MTZ for 2–3 Ga may be the

mantle source of lamproites from Gaussberg. Kuritani et al. (2011) proposed that the MTZ, metasomatized by involvement of ancient (>1 Ga) and recent sediment from a subducted slab, can explain the high Ba/Th and $^{207}Pb/^{206}Pb$ ratios of the Cenozoic basalts in NE China. Wang et al. (2015) found that contribution of gabbroic components from stagnant slabs in the MTZ significantly affected the chemical and oxygen isotopic values of continental flood basalts. Moreover, Wang et al. (2017) proposed that recycled ancient carbonate-bearing sediments, subducted into the mantle transition zone could form the EM1 reservoir of potassic basalts. Therefore, the present work, together with previous studies, suggests that the MTZ can sequester subducted components without being admixed into the convecting mantle for long periods of time, and thus form distinct mantle reservoirs for the generation of intraplate basalts.

6. Conclusions

Our geochemical results from bulk rock, olivine and melt inclusions of Jurassic mafic lavas in South China provide a new perspective on the origin of HIMU-like basalt. The following conclusions can be summarized:

(1) The H_2O content of melt inclusion was mainly affected by post-entrapment crystallization and kinetic diffusion through host olivine and can also be influenced by magmatic degassing for low-Fo olivine-hosted melt inclusion. Using the least-affected melt inclusion that has the highest water content (up to 5.0 wt%) and mantle-like δD value, the primary magma of the Antang basalts is estimated to have H_2O ≥2.65 wt% and the corresponding mantle source has H_2O concentration between 0.14 and 0.22 wt%. The low δD values in the water-rich melt inclusions indicate that water within the source is principally primordial.

(2) The Antang basalts were derived from a hydrous MTZ composed mainly of recycled oceanic slabs that had stagnated for over 1.0 Ga. The dominant mantle lithology was eclogite or pyroxenite.

(3) The hydrous mantle transition zone is a potential source for generation of compositionally diverse and unusually volatile-rich intraplate basalts.

Supplementary data to this article can be found online at https://doi.org/10.1016/j.lithos.2019.105337.

Acknowledgements

Declaration of Competing Interests

The authors declare that they have no known competing financial interests or personal relationships that could have appeared to influence the work reported in this paper.

References

Agrusta, R., Goes, S., van Hunen, J., 2017. Subducting-slab transition-zone interaction: stagnation, penetration and mode switches. Earth Planet. Sci. Lett. 464, 10–23.

Bolfan-Casanova, N., Mackwell, S., Keppler, H., McCammon, C., Rubie, D.C., 2002. Pressure dependence of H solubility in magnesiowustite up to 25 GPa: implications for the storage of water in the Earth's lower mantle. Geophys. Res. Lett. 29, 1029–1032.

Bolfan-Casanova, N., Keppler, H., Rubie, D.C., 2003. Water partitioning at 660 km depth and evidence for very low water solubility in magnesium silicate perovskite. Geophys. Res. Lett. 30. https://doi.org/10.1029/2003GL017182.

Chauvel, C., Hofmann, A.W., Vidal, P., 1992. HIMU-EM: the French-Polynesian connection. Earth Planet. Sci. Lett. 110, 99–119.

Chen, J.H., 2016. Lower-mantle materials under pressure. Science 351, 122–123.

Chen, Y., Provost, A., Schiano, P., Cluzel, N., 2011. The rate of water loss from olivine-hosted melt inclusions. Contrib. Mineral. Petrol. 162, 625–636.

Conrad, C.P., Bianco, T.A., Smith, E.I., Wessel, P., 2011. Patterns of intraplate volcanism controlled by asthenospheric shear. Nat. Geosci. 4, 317–321.

Danyushevsky, L., Plechov, P., 2011. Petrolog3: Integrated software for modelling crystallization processes. Geochem. Geophys. Geosyst. 12. https://doi.org/10.1029/2011GC003516.

Danyushevsky, L.V., Della-Pasqua, F.N., Sokolov, S., 2000. Re-equilibration of melt inclusions trapped by magnesian olivine phenocrysts from subduction-related magmas: petrological implications. Contrib. Mineral. Petrol. 138, 68–83.

Dixon, J.E., Leist, L., Langmuir, C., Schilling, J.G., 2002. Recycled dehydrated lithosphere observed in plume-influenced mid-ocean-ridge basalt. Nature 420, 385–389.

Faccenna, C., Becker, T.W., Lallemand, S., Lagabrielle, Y., Funiciello, F., Piromallo, C., 2010. Subduction-triggered magmatic pulses: a new class of plumes? Earth Planet. Sci. Lett. 299, 54–68.

Gaetani, G.A., O'Leary, J.A., Shimizu, N., Bucholz, C.E., Newville, M., 2012. Rapid reequilibration of H_2O and oxygen fugacity in olivine-hosted melt inclusions. Geology 40, 915–918.

Gao, S., Yang, J., Zhou, L., Li, M., Hu, Z., Guo, J., Yuan, H., Gong, H., Xiao, G., Wei, J., 2011. Age and growth of the Archean Kongling terrain, South China, with emphasis on 3.3 Ga granitoid gneisses. Am. J. Sci. 311, 153–182.

Guo, F., Guo, J.T., Wang, C.Y., Fan, W.M., Li, C.W., Zhao, L., Li, H.X., Li, J.Y., 2013. Formation of mafic magmas through lower crustal AFC processes: an example from the Jinan gabbroic intrusion in the North China Block. Lithos 179, 157–174.

Hanyu, T., Tatsumi, Y., Senda, R., Miyazaki, T., Chang, Q., Hirahara, Y., Takahashi, T., Kawabata, H., Suzuki, K., Kimura, J.I., Nakai, S., 2011. Geochemical characteristics and origin of the HIMU reservoir: a possible mantle plume source in the lower mantle. Geochem. Geophys. Geosyst. 12. https://doi.org/10.1029/2010GC003252.

Hauri, E.H., 2002. SIMS analysis of volatiles in silicate glasses, 2: isotopes and abundances in Hawaiian melt inclusions. Chem. Geol. 183, 115–141.

Hauri, E.H., Gaetani, G.A., Green, T.H., 2006. Partitioning of water during melting of the Earth's upper mantle at H_2O-undersaturated conditions. Earth Planet. Sci. Lett. 248, 715–734.

Herzberg, C., 2011. Identification of source lithology in the Hawaiian and Canary Islands: implications for origins. J. Petrol. 52, 113–146.

Hoernle, K., White, J.D.L., van den Bogaard, P., Hauff, F., Coombs, D.S., Werner, R., Timm, C., Garbe-Schonberg, D., Reay, A., Cooper, A.F., 2006. Cenozoic intraplate volcanism on New Zealand: upwelling induced by lithospheric removal. Earth Planet. Sci. Lett. 248, 350–367.

Hofmann, A.W., 1997. Mantle geochemistry: the message from oceanic volcanism. Nature 385, 219–229.

Hu, S., Lin, Y.T., Zhang, J.C., Hao, J.L., Yang, W., Deng, L.W., 2015. Measurements of water content and D/H ratio in apatite and silicate glasses using a NanoSIMS 50L. J. Anal. At. Spectrom. 30, 967–978.

Hu, S., Lin, Y.T., Zhang, J.C., Hao, J.L., Yamaguichi, A., Zhang, T., Yang, W., Changela, H., 2019. Volatiles in the martian crust and mantle: clues from the NWA 6162 shergottite. Earth Planet. Sci. Lett. https://doi.org/10.1016/j.epsl.2019.115902.

Huang, X.G., Xu, Y.S., Karato, S.I., 2005. Water content in the transition zone from electrical conductivity of wadsleyite and ringwoodite. Nature 434, 746–749.

Irifune, T., Rinwood E., A., 1993. Phase relationships in subducted oceanic crust and buoyancy relationships at depths of 600-800 km in the mantle. Earth and Planetary Science Letters 117, 101–110.

Ishikawa, A., Senda, R., Suzuki, K., Dale, C.W., Meisel, T., 2014. Re-evaluation of digestion methods for highly siderophile element and ^{187}Os analysis: evidence from geological reference materials. Chem. Geol. 384, 27–46.

Karato, S.I., 2010. Water distribution across the mantle transition zone and its implications for global material circulation. Earth Planet. Sci. Lett. 301, 413–423.

Klemme, S., Blundy, J.D., Wood, B.J., 2002. Experimental constraints on major and trace element partitioning during partial melting of eclogite. Geochim. Cosmochim. Acta 66, 3109–3123.

Kogiso, T., Hirschmann, M.M., 2006. Partial melting experiments of bimineralic eclogite and the role of recycled mafic oceanic crust in the genesis of ocean island basalts. Earth Planet. Sci. Lett. 249, 188–199.

Kuritani, T., Ohtani, E., Kimura, J.I., 2011. Intensive hydration of the mantle transition zone beneath China caused by ancient slab stagnation. Nat. Geosci. 4, 713–716.

Kogiso, T., Tatsumi, Y., Shimoda, G., Barsczus, H.G., 1997a. High μ (HIMU) ocean island basalts in southern Polynesia: new evidence for whole mantle scale recycling of subducted oceanic crust. J. Geophys. Res. 102, 8085–8103.

Kogiso, T., Tatsumi, Y., Nakano, S., 1997b. Trace element transport during dehydration processes in the subducted oceanic crust: 1. experiments and implications for the origin of ocean island basalts. Earth Planet. Sci. Lett. 148, 193–205.

Kuritani, T., Kimura, J.I., Ohtani, E., Miyamoto, H., Furuyama, K., 2013. Transition zone origin of potassic basalts from Wudalianchi volcano, northeast China. Lithos 156, 1–12.

Kuritani, T., Xia, Q.K., Kimura, J., Liu, J., Shimizu, K., Ushikubo, T., Zhao, D.P., Nakagawa, M., Yoshimura, S., 2019. Buoyant hydous mantle plume from the mantle transition zone. Sci. Rep. 9. https://doi.org/10.1038/s41598-019-43103-y.

Li, J., Jiang, X.Y., Xu, J.F., Zhong, L.F., Wang, X.C., Wang, G.Q., Zhao, P.P., 2014. Determination of Platinum-Group Elements and Re-Os Isotopes using ID-ICP-MS and N-TIMS from a Single Digestion after Two-Stage Column Separation. Geostand. Geoanal. Res. 38, 37–50.

Li, X.H., Li, W.X., Li, Z.X., Lo, C.H., Wang, J., Ye, M.F., Yang, Y.H., 2009. Amalgamation between the Yangtze and Cathaysia Blocks in South China: constraints from SHRIMP U–Pb zircon ages, geochemistry and Nd–Hf isotopes of the Shuangxiwu volcanic rocks. Precambrian Res. 174, 117–128.

Li, X.H., Li, Z.X., He, B., Li, W.X., Li, Q.L., Gao, Y.Y., Wang, X.C., 2012. The Early Permian active continental margin and crustal growth of the Cathaysia Block: In situ U-Pb, Lu-Hf and O isotope analyses of detrital zircons. Chem. Geol. 328, 195–207.

Liu, C.Z., Liu, Z.C., Wu, F.Y., Chu, Z.Y., 2012. Mesozoic accretion of juvenile sub-continental lithospheric mantle beneath South China and its implications: geochemical and Re-Os isotopic results from Ningyuan mantle xenoliths. Chem. Geol. 291, 186–198.

Mattey, D., Lowry, D., Macpherson, C., 1994. Oxygen isotope composition of mantle peridotite. Earth Planet. Sci. Lett. 128, 231–241.

McKeegan, K.D., Aleon, J., Bradley, J., Brownlee, D., Busemann, H., Butterworth, A., Chaussidon, M., Fallon, S., Floss, C., Gilmour, J., 2006. Isotopic compositions of cometary matter returned by Stardust. Science 314, 1724–1728.

Meibom, A., Sleep, N.H., Chamberlain, C.P., Coleman, R.G., Frei, R., 2002. Re-Os isotopic evidence for long-lived heterogeneity and equilibration processes in the Earth's upper mantle. Nature 419, 705–708.

Meier, U., Trampert, J., Curtis, A., 2009. Global variations of temperature and water content in the mantle transition zone from higher mode surface waves. Earth Planet. Sci. Lett. 282, 91–101.

Michael, P., 1995. Regionally distinctive sources of depleted MORB: evidence from trace elements and H_2O. Earth Planet. Sci. Lett. 131, 301–320.

Miyagi, I., Matsubaya, O., 2003. Hydrogen isotopic composition of hornblende and biotite phenocrysts from Japanese Island arc volcanoes; evaluation of alteration process of the hydrogen isotopic ratios by degassing and re-equilibration. J. Volcanol. Geotherm. Res. 126, 157–168.

Murphy, D.T., Collerson, K.D., Kamber, B.S., 2002. Lamproites from Gaussberg, Antarctica: possible transition zone melts of Archaean subducted sediments. J. Petrol. 43, 981–1001.

Nebel, O., Arculus, R.J., van Westrenen, W., Woodhead, J.D., Jenner, F.E., Nebel-Jacobsen, Y.J., Eggins, S.M., 2013. Coupled Hf-Nd-Pb isotope co-variations of HIMU oceanic island basalts from Mangaia, Cook-Austral islands, suggest an Archean source component in the mantle transition zone. Geochim. Cosmochim. Acta 112, 87–101.

Pamato, M.G., Myhill, R., Ballaran, T.B., Frost, D.J., Heidelbach, F., Miyajima, N., 2015. Lower-mantle water reservoir implied by the extreme stability of a hydrous aluminosilicate. Nat. Geosci. 8, 75–79.

Panter, K.S., Blusztajn, J., Hart, S.R., Kyle, P.R., Esser, R., Mclntosh, W.C., 2006. The origin of HIMU in the SW Pacific: evidence from intraplate volcanism in southern New Zealand and subantarctic islands. J. Petrol. 47, 1673–1704.

Pearson, D.G., Brenker, E.E., Nestola, F., McNeill, J., Nasdala, L., Hutchison, M.T., Matveev, S., Mather, K., Silversmit, G., Schmitz, S., 2014. Hydrous mantle transition zone indicated by ringwoodite included within diamond. Nature 507, 221–224.

Pertermann, M., Hirschmann, M.M., Hametner, K., Gunther, D., Schmidt, M.W., 2004. Experimental determination of trace element partitioning between garnet and silica-rich liquid during anhydrous partial melting of MORB-like eclogite. Geochem. Geophys. Geosyst. 5. https://doi.org/10.1029/2003GC000638.

Peucker-Ehrenbrink, B., Hanghoj, K., Atwood, T., Kelemen, P.B., 2012. Rhenium–osmium isotope systematics and platinum group element concentrations in oceanic crust. Geology 40, 199–202.

Pilet, S., Baker, M.B., Stolper, E.M., 2008. Metasomatized lithosphere and the origin of alkaline lavas. Science 320, 916–919.

Poli, S., Schmidt, M.W., 2002. Petrology of subducted slabs. Annu. Rev. Earth Planet. Sci. 30, 207–235.

Reisberg, L., Meisel, T., 2002. The Re-Os isotopic system: a review of analytical techniques. Geostand. Newslett. 26, 249–267.

Ringwood, A.E., 1994. Role of the transition zone and 660 km discontinuity in mantle dynamics. Phys. Earth Planet. Inter. 86, 5–24.

Saal, A.E., Hauri, E.H., Langmuir, C.H., Perfit, M.R., 2002. Vapour undersaturation in primitive mid-ocean-ridge basalt and the volatile content of Earth's upper mantle. Nature 419, 451–455.

Shaw, A.M., Hauri, E.H., Fischer, T.P., Hilton, D.R., Kelley, K.A., 2008. Hydrogen isotopes in Mariana arc melt inclusions: implications for subduction dehydration and the deep-Earth water cycle. Earth Planet. Sci. Lett. 275, 138–145.

Shaw, A.M., Hauri, E.H., Behn, M.D., Hilton, D.R., Macpherson, C.G., Sinton, J.M., 2012. Long-term preservation of slab signatures in the mantle inferred from hydrogen isotopes. Nat. Geosci. 5, 224–228.

Sobolev, A.V., Hofmann, A.W., Kuzmin, D.V., Yaxley, G.M., Arndt, N.T., et al., 2007. The amount of recycled crust in sources of mantle-derived melts. Science 316, 412–417.

Stracke, A., Bizimis, M., Salters, V.J.M., 2003. Recycling oceanic crust: quantitative constraints. Geochem. Geophys. Geosyst. 4. https://doi.org/10.1029/2001GC000223.

Sun, S.S., McDonough, W.F., 1989. Chemical and isotopic systematics of oceanic basalts: implication for mantle composition and processes. In: Saunder, A.D., Norry, M.J. (Eds.), Magmatism in the Ocean Basins, 42. Geological Society of London, Special Publication, London, pp. 313–345.

Thirlwall, M.F., 1997. Pb isotopic and elemental evidence for OIB derivation from young HIMU mantle. Chem. Geol. 139 (51–47).

Thompson, R.N., Ottley, C.J., Smith, P.M., Pearson, D.G., Dickin, A.P., Morrison, M.A., Leat, P.T., Gibson, S.A., 2005. Source of the quaternary alkalic basalts, picrites and basanites of the Potrillo Volcanic Field, New Mexico, USA: lithosphere or convecting mantle? J. Petrol. 46, 1603–1643.

Vinnik, L., Farra, V., 2007. Low S velocity atop the 410-km discontinuity and mantle plumes. Earth Planet. Sci. Lett. 262, 398–412.

Wang, X.C., Wilde, S.A., Li, Q.L., Yang, Y.N., 2015. Continental flood basalts derived from the hydrous mantle transition zone. Nat. Commun. 6. https://doi.org/10.1038/ncomms8700.

Wang, X.C., Wilde, S.A., Xu, B., Pang, C.J., 2016. Origin of arc-like continental basalts: implications for deep-Earth fluid cycling and tectonic discrimination. Lithos 261, 5–45.

Wang, X.J., Chen, L.H., Hofmann, A.W., Mao, F.G., Liu, J.Q., Zhong, Y., Xie, L.W., Yang, Y.H., 2017. Mantle transition zone-derived EM1 component beneath NE China: geochemical evidence from Cenozoic potassic basalts. Earth Planet. Sci. Lett. 465, 16–28.

Wang, Y.J., Liao, C.L., Fan, W.M., Peng, T.P., 2004. Early Mesozoic OIB-type alkaline basalt in central Jiangxi Province and its tectonic implications. Geochimica 33, 109–117 (in Chinese with English abstract).

Wang, Y.J., Fan, W.M., Cawood, P.A., Li, S.Z., 2008. Sr-Nd-Pb isotopic constraints on multiple mantle domains for Mesozoic mafic rocks beneath the South China block hinterland. Lithos 106, 297–308.

Wang, Z.R., Gaetani, G.A., 2008. Partitioning of Ni between olivine and siliceous eclogite partial melt: experimental constraints on the mantle source of Hawaiian basalts. Contrib. Mineral. Petrol. 155, 661–678.

Weaver, B.L., 1991. The origin of ocean island basalt end-member compositions-trace element and isotopic constraints. Earth Planet. Sci. Lett. 104, 381–397.

Weis, D., Kieffer, B., Maerschalk, C., Pretorius, W., Barling, J., 2005. High-precision Pb-Sr-Nd-Hf isotopic characterization of USGS BHVO-1 and BHVO-2 reference materials. Geochem. Geophys. Geosyst. 6. https://doi.org/10.1029/2004GC000852.

Weiss, Y., Class, C., Goldstein, S.L., Hanyu, T., 2016. Key new pieces of the HIMU puzzle from olivines and diamond inclusions. Nature 537, 666–670.

Xia, Q.K., Liu, J., Kovács, I., Hao, Y.T., Li, P., Yang, X.Z., Chen, H., Sheng, Y.M., 2019. Water in the upper mantle and deep crust of eastern China: concentration, distribution and implications. Natl. Sci. Rev. 6, 125–144.

Xu, Z., Zheng, Y.F., Zhao, Z.F., Gong, B., 2014. The hydrous properties of subcontinental lithospheric mantle: Constraints from water content and hydrogen isotope composition of phenocrysts from Cenozoic continental basalts in North China. Geochim. Cosmochim. Acta 143, 285–302.

Yu, J., O'Reilly, Y.S., Wang, L., Griffin, W.L., Jiang, S., Wang, R., Xu, X., 2007. Finding of ancient materials in Cathaysia and implication for the formation of Precambrian crust. Chin. Sci. Bull. 52, 13–22.

Zeng, G., Chen, L.H., Xu, X.S., Jiang, S.Y., Hofmann, A.W., 2010. Carbonated mantle sources for Cenozoic intra-plate alkaline basalts in Shandong, North China. Chem. Geol. 273, 35–45.

Zeng, G., He, Z.Y., Li, Z., Xu, X.S., Chen, L.H., 2016. Geodynamics of paleo-Pacific plate subduction constrained by the source lithologies of Late mesozoic basalts in southeastern China. Geophys. Res. Lett. 143, 10189–10197.

Zhang, H.F., Goldstein, S.L., Zhou, X.H., Sun, M., Zheng, J.P., Cai, Y., 2008. Evolution of subcontinental lithospheric mantle beneath eastern China: Re-Os isotopic evidence from mantle xenoliths in Paleozoic kimberlites and Mesozoic basalts. Contrib. Mineral. Petrol. 155, 271–293.

Zhou, X.M., Sun, T., Shen, W.Z., Shu, L.S., Niu, Y.L., 2006. Petrogenesis of Mesozoic granitoids and volcanic rocks in South China: a response to tectonic evolution. Episodes 29, 26–33.

Zindler, A., Hart, S., 1986. Chemical geodynamics. Annu. Rev. Earth Planet. Sci. 14, 493–571.